

Correcting PAR Data from Photovoltaic Quantum Sensors on Remote Weather Stations on the Great Barrier Reef

MANUEL NUNEZ,^a NEAL CANTIN,^b CRAIG STEINBERG,^b VIRGINIE VAN DONGEN-VOGELS,^b AND SCOTT BAINBRIDGE^b

^a *School of Geography, Planning and Spatial Sciences, University of Tasmania, Hobart, Tasmania, Australia*

^b *Australian Institute of Marine Science, Townsville, Queensland, Australia*

(Manuscript received 10 July 2021, in final form 18 October 2021)

ABSTRACT: The study addresses a network of remote weather stations on the Great Barrier Reef (GBR) that house Licor192 quantum sensors measuring photosynthetically active radiation (PAR) above water. There is evidence of significant degradation in the signal from the sensors after a 2-yr deployment. Main sources of uncertainty in the calibration are outlined, which include degradation of the photodiode, soiling of the sensors by dust and salt spray, cosine responses, and sensitivity to air temperature. Raw PAR data are improved using correction factors based on a cloudless PAR model. Uncertainties in cosine responses of the instrument are low but significant errors may occur if the supporting platform is misaligned and not horizontal. A set of recommendations are provided to improve the quality of the PAR data.

SIGNIFICANCE STATEMENT: A method is described to correct historical PAR data collected on the Great Barrier Reef, such that these valuable observations may be improved and used effectively.

KEYWORDS: In situ atmospheric observations; In situ oceanic observations; Instrumentation/sensors; Measurements

1. Introduction


Surface irradiance measurements in marine regions are difficult for various reasons including logistics, maintenance, calibration, and costs. Often wave action transports dust, aerosol salts, and algae suspended in the marine environment to the sensing surface of the radiometer, thus creating an aerosol/salt layer that acts to deplete some of the radiation reaching the sensor (Habte and Sengupta 2016; Johnson et al. 2014; Mant and Pillai 2010). This process changes the calibration over time, requiring constant cleaning of radiometers on oceanic platforms, a task that strains resources in isolated locations. Radiometers installed on ships and mooring systems need to be mounted with uninterrupted sky views, therefore mimicking conditions in the nearby open ocean free of artificial obstructions (Brando et al. 2016; WMO 2008). This may not be achievable in many practical applications, and often additional errors occur due to blockage of solar radiation by obstructions or incorrect levelling of the radiometer sensing surface (Menyhart et al. 2015; MacWhorter and Weller 1991).

Data errors produced by these processes may be substantial and they warrant a reexamination of the approaches used in obtaining solar radiation fluxes from fixed oceanic platforms such as towers and buoys. Ideally, measurements of incoming radiation in isolated and difficult environments could be covered by cheaper but more numerous lower-quality instruments with good quality control routines. The approach is

justified as a network of radiometers is well suited for sampling spatial and temporal variability in surface irradiance responding to changes in atmospheric constituents—aerosols and clouds (Madhavan et al. 2017; Schenk et al. 2015). However, degradation of these cheaper instruments may be prevalent. Given the logistical difficulties of frequent replacement, it is useful to examine the feasibility of detecting and correcting data for possible errors between calibrations.

The Australian Institute of Marine Sciences (AIMS) has maintained a network of weather stations over the Great Barrier Reef (GBR) (Fig. 1 and Table 1; Bainbridge 2017) since the late 1980s, which also include measurements of photosynthetically active radiation (PAR) using LICOR192 quantum sensors (<https://www.licor.com/env/products/light/quantum.html>). The instruments are nominally replaced every two years with newly calibrated instruments, but often replacement periods are longer depending on ship logistics and other priorities. Useful high-quality data rely on valid and frequent calibrations, a laborious and often impractical task in oceanic environments. For pyranometers, they involve laboratory or field calibrations where the sensor is compared with a standard instrument or standard lamp [WMO 2008; Forgan 1996; International Organization for Standardization (ISO); ISO 1993]. The calibrated data may be used with confidence provided there has been no signal degradation between calibrations. Often this is not the case and in this study we explore a practical approach to monitor and correct the signal output by referencing the signals to a radiative transfer model. These corrections may be applied to either historical data or in real time depending on the method of acquisition.

The subsequent sections of the manuscript describe various aspects of the need to, and approaches for, correcting PAR observations. The need for corrections is discussed in section 1.

 Denotes content that is immediately available upon publication as open access.

Corresponding author: Manuel Nunez, m.nunez@utas.edu.au

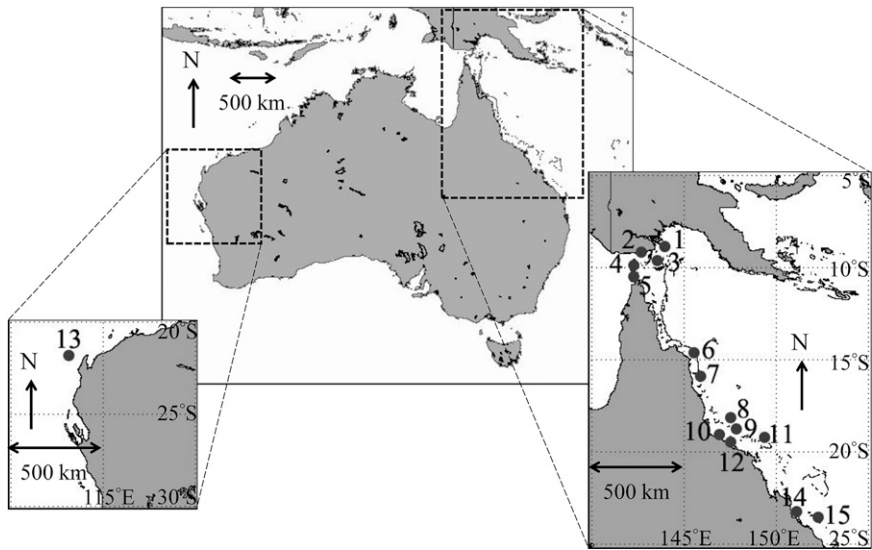


FIG. 1. Map of northern Australia showing the locations of the weather stations recording PAR. Each number in the map represents a specific weather station as shown in Table 1.

Section 2 outlines how the Licor quantum sensor functions, standard calibration techniques, and typical instrumental errors. Section 3 discusses the radiative transfer model, its validation with measured data, and how the correction process is applied. Section 4 compares a Licor corrected with our technique against high-quality measured PAR data. Section 5 is a discussion of results, mainly outlining the usefulness and applicability of the technique. Finally, the outstanding points of the study are summarized in section 6.

2. Data acquisition

a. Licor 192 underwater quantum sensor

By definition, spectral solar irradiance at Earth’s surface E_{λ} ($\text{W m}^{-2} \text{ nm}^{-1}$) defines the incoming solar radiant energy crossing a unit horizontal surface per unit of time in a narrow

wavelength interval (Iqbal 1983). Quantum irradiance measures PAR in photon units, which may be defined as (see appendix)

$$\text{PAR}(\mu\text{mol m}^{-2} \text{ s}^{-1}) = C' \int_{400}^{700} E_{\lambda} \lambda d\lambda, \tag{1}$$

where C' is a constant given as 0.0008362 and λ is wavelength (nm). Silicon sensors are popular to measure solar radiation for their high current output, rapid response time, low dark current, and wide sensitivity to solar wavelengths [see Table 2 and publications by Kerr et al. (1967) and McPherson (1969)]. Quantum sensors such as the LI192 use a silicon photodiode in combination with a glass optical filter ensuring a linearly increasing response between 400 and 700 nm and zero elsewhere. This design mimics the wavelength dependence as seen inside the integral of Eq. (1), therefore minimizing errors with incoming PAR (Licor 1992; McPherson 1969; Fig. 2).

TABLE 1. Weather stations managed by the Australian Institute of Marine Sciences, which record 10-min PAR.

Station No.	Station	Location	Start date
1	Bramble Cay	9.142°S, 143.876°E	July 2015
2	Saibai Island	9.388°S, 142.632°E	April 2016
3	Masig Island	9.760°S, 143.401°E	June 2013
4	Badu Island	10.157°S, 142.162°E	May 2018
5	Thursday Island	10.595°S, 142.220°E	January 2012
6	Lizard Island	14.691°S, 145.466°E	February 2012
7	Agincourt Reef	15.983°S, 145.822°E	March 1991
8	Myrmidon Reef	18.274°S, 147.382°E	November 1987
9	Davies Reef	18.832°S, 147.634°E	October 1991
10	Cleveland Bay	19.139°S, 146.899°E	December 1999
11	Hardy Reef	19.186°S, 149.183°E	June 1989
12	Cape Bowling Green	19.305°S, 147.393°E	July 1987
13	Ningaloo Reef	22.029°S, 113.122°E	February 1997
14	Square Rocks	23.099°S, 150.886°E	July 2000
15	Heron Island	23.440°S, 151.980°E	September 2012

TABLE 2. ISO criteria for pyranometer classification (ISO document 9060).

	First class	Second class	Licor quantum sensor
Time for 95% response	<10 s	<30 s	<1 μ s
Zero offset due to both radiation and temperature	$\pm 21 \text{ W m}^{-2}$	$\pm 41 \text{ W m}^{-2}$	<1 $\mu\text{mol m}^{-2} \text{s}^{-1}$
Percentage change in responsivity per year	$\pm 1.5\%$	$\pm 3.0\%$	On occasions >10%
Nonlinearity percentage change in responsivity from 500 to 1000 W m^{-2}	$\pm 1.5\%$	$\pm 3.0\%$	< $\pm 1\%$ up to $10^4 \mu\text{mol m}^{-2} \text{s}^{-1}$
Errors introduced by spectral instrument response	$\pm 1.5\%$	$\pm 5.0\%$	<1% (Ross and Sulev 2000)
Temperature response (-10° to 40°C)	$\pm 2.0\%$	$\pm 4.0\%$	$\pm 3\%$ from std temperature of calibration
Cosine error from horizontal	$\pm 2.0\%$	$\pm 5.0\%$	<5% at incidence angles less than 70°

Several design features improve the signal quality. An acrylic diffuser channels the light into a vertical shaft containing the sensor/filter combination. The diffusing head slightly protrudes, absorbing solar radiation from the sides and countering reflection losses from the top at high solar zenith angle. A raised circular lip at the edge minimizes absorption at very large zenith angles by blocking some of the light (Kerr et al. 1967; Licor 1992). King and Myers (1997) and Michalsky et al. (1995) estimated cosine errors for a range of Licor sensors including the LI192. The authors show that errors associated are small and less than 5% in the solar zenith angle range from 0° to 75° .

In this study we determine cosine errors for four instruments using laboratory facilities at In-situ Marine Optics, Perth, Western Australia. The instruments are placed in a rotating stand and exposed to a laser source operating at 532 nm. The angle of incidence for the expanded light beam changes as the rotating stand changes position. A range of signals are obtained covering incidence angles from -90° to $+90^\circ$. Normalizing the instrument response to “1” at 0° incidence angle, the cosine error (CE) may be defined as in Eq. (2):

$$\text{CE}(\theta) = \text{Signal}(\theta) / \cos(\theta). \quad (2)$$

Figure 3 shows CE as a function of incidence angle for four different sensors. In general, absolute errors are under 5% in the zenith angle range of -70° to $+70^\circ$, but rapidly increase past 80° . The CE pattern is slightly nonsymmetrical around 0° , a feature that also appears in Michalsky et al. (1995) for the Licor quantum sensor (their Fig. 4c).

Table 2 summarizes various features of the LI192 as reported by the manufacturer and from the literature including this work (Licor 1992; King et al. 1998; King and Myers 1997; Michalsky et al. 1995, 1991; Ross and Sulev 2000). Being a solid-state device, the response time is rapid ($<1 \mu\text{s}$) and it can monitor high frequency variability in PAR induced by cloud cover. The zero offset is small at less than $1 \mu\text{mol m}^{-2} \text{s}^{-1}$, which contrasts with thermopile pyranometers where emission from glass domes can be a substantial source of offset error (Ji 2007; Dutton et al. 2001). Cosine errors and related azimuthal errors (Fig. 3) have a maximum of around 5% for angles of incidence less than 80° .

The sensor signal is strongly linear with PAR, a feature that will be used in this study. Ross and Sulev (2000) show that errors caused by spectral changes in solar irradiance during the day will produce errors of less than 1% in estimates of PAR from the Licor quantum sensor. Additionally, cloud effects will not affect the linearity of the signals as cloud

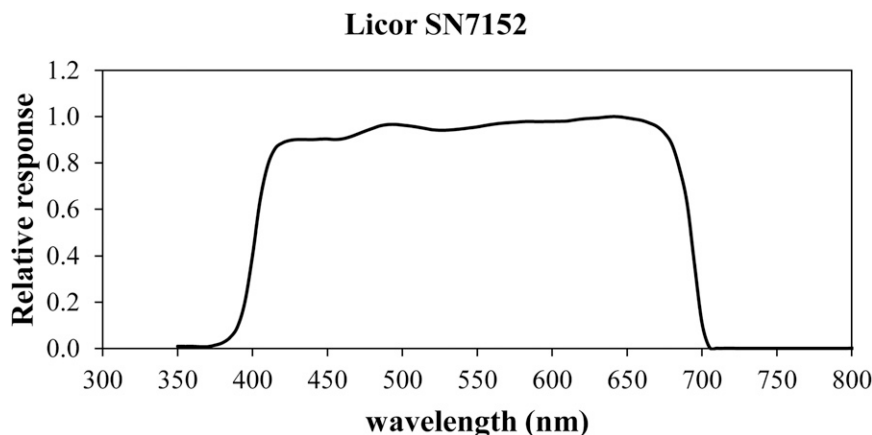


FIG. 2. Spectral response of Licor serial number (SN) 7152 quantum sensor obtained from laboratory calibration. Data have been normalized to a maximum value of 1. A Lambda Scientific LEOI-94 monochromator has been used in combination with a tungsten-bromine lamp and a reference photodiode (Thorlabs FDS100). Data have been provided by In-situ Marine Optics Pty. Ltd.

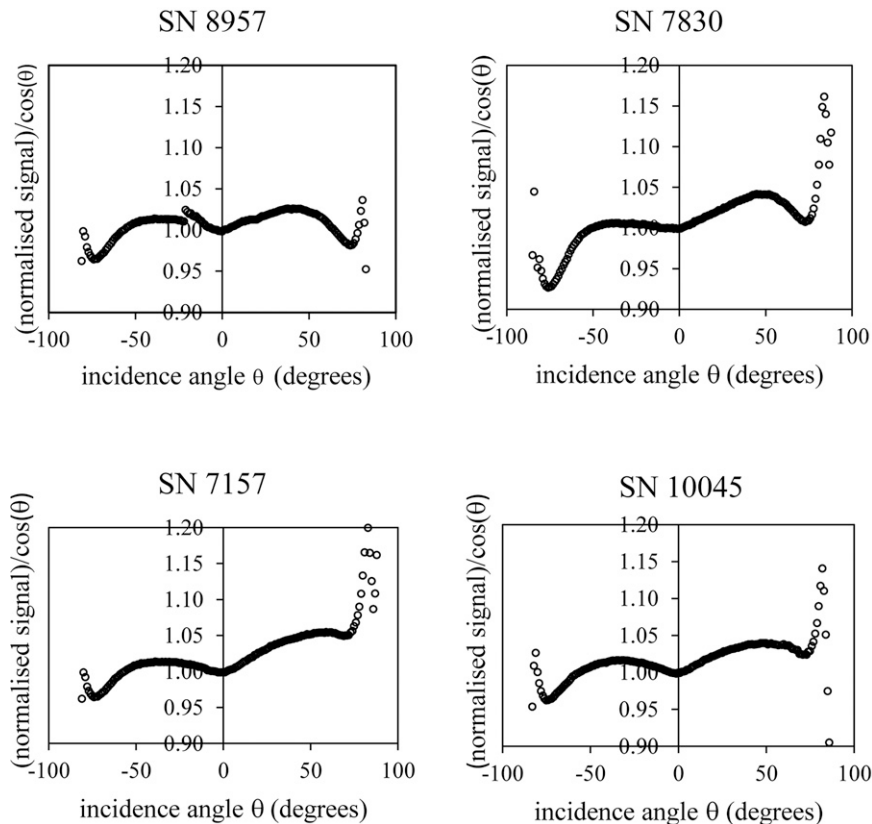


FIG. 3. Cosine response of four quantum sensors when exposed to a laser source operating at 532 nm. For a perfect cosine response, the normalized response [normalized signal/cos(θ)] would equal 1. Data provided courtesy of In-situ Marine Optics.

transmission is slowly varying over wavelength, varying by a few percent over the PAR wavelengths (Serrano et al. 2015; Stephens 1994; Kylling et al. 1997).

Changes in responsivity due to temperature and yearly degradation are substantial. According to the manufacturer (Licor 1992), a maximum uncertainty of $\pm 0.15^\circ\text{C}$ per degree is expected at temperatures different from the calibration temperature of 25°C . Raich et al. (2007), King et al. (1998), and Michalsky et al. (1991) have developed correction factors that may be applied to Licor silicon pyranometers based on instrumental temperatures. Licor quantum sensors do not record temperatures as a standard product and seasonal changes in responsivity could occur. This potential source of uncertainty needs correction factors, which are able to address responsivity changes occurring at short time scales perhaps responding to instrumental temperatures or other processes.

Sensor drift changes are given as less than $\pm 2\% \text{ yr}^{-1}$ (Licor 1992) under normal conditions and with proper maintenance and cleaning of the sensors. These conditions are often not met in oceanic environments where sensors are unattended and exposed to the elements for long periods. On occasions, a signal change as high as $10\% \text{ yr}^{-1}$ has been found in our study, a result of not only instrument signal degradation but of other factors as well related to the stability of the platform,

fouling of the sensing surface or even incorrect programming of the datalogger. These issues will be discussed in the next sections.

b. Deployment and calibration

AIMS maintains a network of automated near-real-time weather stations along the GBR and into Torres Strait with 15 of these having above water PAR sensors (Table 1). These stations deploy a LI-COR LI-192 Underwater Quantum Sensor using factory-supplied “in-air” calibrations. The instruments are positioned on fixed and rigid platforms either on a 6-m-high reef-mounted pole or a larger 10-m tower, on tourist pontoons or other available infrastructure. Ideally sensors installed in marine platforms should be at 10-m height above mean sea level, which correspond to WMO recommendations for wind sensors (WMO 2008). However, in most cases due to practical considerations the instruments are fixed at lower elevations but not lower than 6 m from mean sea level. This elevation provides some protection from sea spray and other aerosols. Care has been taken to ensure a minimum of obstructions in the sensor field of view and a levelling sensing surface as per WMO guidelines (WMO 2008). The sensors are levelled using custom made mounts, but on moored platforms, such as tourist

pontoons, it is not possible to ensure the sensors are always perfectly horizontal.

The sensors are interfaced to a Campbell Scientific CR1000 logger with a logging rate of 1 Hz and an integration time of 10 min. There is direct two-way communication back to AIMS with integrated data being retrieved every 10 min, thus providing near real time measurements of reef-based PAR. The data are available via the AIMS Weather Station website (www.aims.gov.au/docs/data/data.html). Instruments are nominally replaced every 2 years corresponding to factory recommendation (Licor 1992). Often replacement periods are longer due to practical considerations involving priorities in ship time, time of year, and disruption by extreme weather events such as tropical cyclones. The replaced instruments are then sent to the Licor for recalibration.

c. Some evidence of signal degradation in the PAR instruments

Cloudless days were selected so as to examine the instrument performance in more simple conditions. Selection was based on satellite data (www.worldview.earthdata.nasa.gov) and the smoothness of the graphical trace on clear days as described in more detail in section 3c(1). In some instances, there are significant deficiencies in both the diurnal pattern of PAR as well as the daily seasonal trends. Under cloudless conditions and with no high aerosol load with low diurnal changes in the GBR region (Masiri et al. 2007; Nunez 1993), it is expected that surface PAR will be symmetrical about solar noon. On occasions this condition is not met as shown in Fig. 4a.

Measured PAR in the morning is noticeably larger than afternoon PAR for Myrmidon Reef during 2019/20 with instrument UWQ99276. This anomaly persisted for all five cloudless days in the dataset, discounting isolated events related perhaps to an aerosol increase in the afternoon. This hysteresis may be explained as either a cosine response that depends on azimuth sun orientation, incorrect leveling upon deployment, or a combination of both effects. All four cosine response curves in Fig. 3 show an azimuth dependence in the cosine response, but differences are not large, less than 5% at zenith angles below 70°. By contrast at 70°, differences in the morning/afternoon PAR are just under 19%, suggesting that levelling errors upon deployment could be partly to blame. For the entire day differences average to 14.9%. Figure 4b shows a graph similar to Fig. 4a, but for Cleveland Bay. The morning/afternoon PAR are very symmetrical with differences under 2% and averaging to 0.6%.

The lack of consistency in the diurnal pattern for cloudless days is to be expected given the different platforms used and the exposed, unattended nature of these sites. Individual deployment on poles might produce errors in the data if the poles depart from a vertical position. By contrast a large structure anchored to a reef will provide a more stable platform, minimizing levelling errors. Additional errors might arise from soiling of the sensor surface as shown for two sensors, a new one and one exposed to the environment for two years (Fig. 5). For pyranometers, various degrees of sensor soiling reduce the output energy by 0.2%–27% (Habte and

Sengupta 2016; Feuermann and Zemel 1993), and deviations from ideal cosine responses can typically decrease or increase by up to 8%–10% depending on the radiation angle of incidence (Michalsky et al. 1991; King and Myers 1997; Patil et al. 2013).

Surface soiling and drift in the instrument electronics will affect not just the diurnal signal but the daily total as well. Licor (1992) lists the calibration to be stable to within $\pm 2\%$ yr⁻¹. However, the accuracy of measured solar radiation is linked to the normal environmental conditions that the instrument is exposed to (ISO 2018), and in the case of the LI192 some form of regular maintenance is assumed. Long-term degradation may be observed in Fig. 6, which shows daily PAR for instrument UWQ8392 deployed at Masig Island (9.760°S, 143.401°E). The instrument underwent a minimum of maintenance and no recalibration since its deployment in July 2013. Monthly average PAR shows yearly seasonality with maxima in the summer months superimposed on a yearly downward trend. A regression of the data gives a yearly decay of 2.73 mol m⁻² day⁻¹, which corresponds to 10.1% of the long-term daily average.

The issue of bird disturbance could potentially affect the signal degradation, although this is unlikely. All marine PAR stations were fitted with bird deterrents for PAR sensors. Our experience is that they have had limited success as birds tend to break the rods. It is straightforward to note if a bird were perched on the sensor as the signal would jump to zero or close to it. It is not frequent and can be easily detected in the records. Field checks on the sensors during replacement and during normal operations reveal no bird deposition on the sensors.

3. Correcting raw PAR data

a. Correction equations

The approach consists of using a validated PAR model for cloudless conditions as a reference to correct for both diurnal and long-term daily trends. For any solar zenith angle z , a corrected PAR (PAR_{corr}) may be written as the product of two correction terms: $c1$, which depends on days after deployment (d), and a second correction $c2$, which is independent of deployment date but only depends on zenith angle (z):

$$\text{PAR}_{\text{corr}}(d, z) = \text{PAR}_{\text{raw}} \times c1(d) \times c2(z), \quad (3a)$$

$$c1(d) = \frac{(\text{PAR}_{\text{mod}})_{\text{noon}}}{(\text{PAR}_{\text{raw}})_{\text{noon}}}. \quad (3b)$$

These two corrections are developed on cloudless days and applied to all 10-min data as in Eq. (3a). It is expected that close to deployment dates $c1 \approx 1.0$ and will increase/decrease as the measurement period (d) progresses. Estimating $c1$ at solar noon is convenient as z is minimum and cosine error effects are also minimized (Fig. 3). The final expression for $c1$ will involve some linear or nonlinear function of d , which is fitted to the data, and which will be applicable for all days of the measurement period.

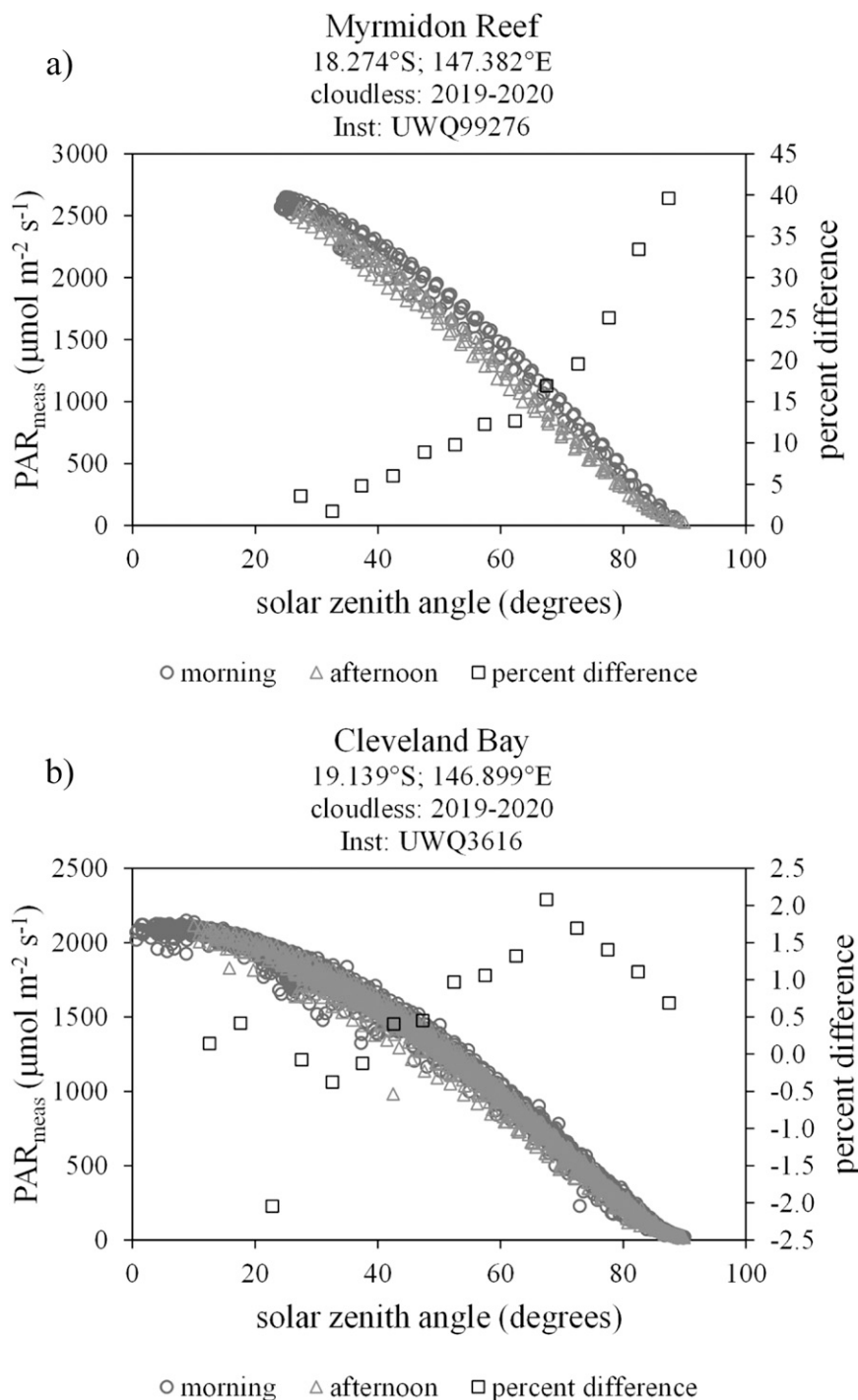


FIG. 4. Cloudless PAR for morning and afternoon vs solar zenith angle in years 2019/20 for (a) Myrmidon Reef and (b) Cleveland Bay. Also shown are the percentage differences between the two datasets when averaged over 5° intervals: $100 \times (\text{PAR}_{\text{morn}} - \text{PAR}_{\text{aft}}) / \text{PAR}_{\text{morn}}$.

Correction for zenith angle (c2) is assumed constant for the measurement period but changes throughout the cloudless day with z . This diurnal correction is performed once the raw signals are corrected for long-term changes as per c1. In this

part of the analysis we use a radiative transfer model to examine the sensitivity of the PAR signal to cosine responses shown in Fig. 3. Finally the sensitivity to changes in the deviation of the platform from the horizontal is also examined.



FIG. 5. Two contrasting Licor 192 underwater quantum sensors. The left instrument is new and has never been exposed. The right one has been measuring PAR for 2 years on a platform in the GBR. The entire surface of the exposed instrument is encrusted with salt particles and dirt, which changes the albedo of the acrylic diffuser.

The underlying assumptions behind the approach relate to the applicability of these two corrections, obtained in cloudless conditions to the general case of all-sky conditions. The instrument linearity (Table 2) supports this assumption so that any solar noon corrections will translate linearly to any time of the day and to cloudy days as well. Any change in noontime correction relates well to the change in the slope of the factory calibration as there is no significant change in the intercept and no intercept correction is done (J. Li 2021, personal communication). The second correction $c2(z)$ has also been derived for cloudless conditions and is influenced by the cosine response of the instrument (Fig. 3), the ratio of direct to diffuse irradiance and the platform tilt. In the absence of diffuse irradiance data, $c2(z)$ must be regarded as a coarse approximation, which is able to account for cosine responses in cloudless conditions, although less effective for cloudy cases.

b. Libradtran 1.7 radiative transfer model

The approach assumes a model that can replicate cloudless conditions approximating the instrument calibration accuracy of $\pm 5\%$. Correction relationships for photovoltaic pyranometers have been developed by various authors (Raich et al. 2007; King et al. 1998; King and Myers 1997). They involve spectral estimates of cloudless irradiance using radiative transfer models or polynomial functions. A variety of radiative transfer models have been used to represent solar radiation in photovoltaic research. They range from empirical or semiempirical (Clack 2017; Mondol et al. 2008; De Soto et al. 2006; Myers 2005; Bird 1984) to radiative transfer models (Razagui et al. 2020; Utrillas et al. 1998; Gueymard 2008, 1995). In this study the Libradtran radiative transfer package (Mayer and Kylling 2005) is used due to its wide acceptance and use, its versatility, and its ease of operation. Details follow below.

The UVSPEC module in the Libradtran 1.7 suite of programs has been used to model surface PAR for cloudless skies (Mayer et al. 2020; Mayer and Kylling 2005). UVSPEC is a one-dimensional multilayered plane parallel radiative transfer program using a discrete ordinate method, a six-stream option and correlated- k lowtran absorption. Input data consist of a tropical atmosphere with background stratospheric aerosol conditions (Shettle 1989), a constant broadband surface albedo of 5% typical of an ocean surface (Jin et al. 2004; Payne 1972), and varying precipitable water vapor and tropospheric aerosols. Model outputs were restricted to wavelengths between 400 and 700 nm, therefore covering the PAR region.

Model sensitivity to precipitable water vapor and aerosol optical depth for the study region was next examined. Monthly precipitable water vapor (pwv) and aerosol optical depth (AOD) at 555 nm were selected from the MODIS *Aqua* instrument gridded product (MYDO8_M3.006 obtained at <https://giovanni.gsfc.nasa.gov>). Monthly data, available as $1^\circ \times 1^\circ$ averages, were recorded for each of the 15 weather stations in Table 1. A total of 180 values of pwv and AOD were obtained for the year 2020 (15 stations \times 12 months). For each dataset, the 1st and 99th percentiles and the mean values were chosen and used as input into the model (Table 3).

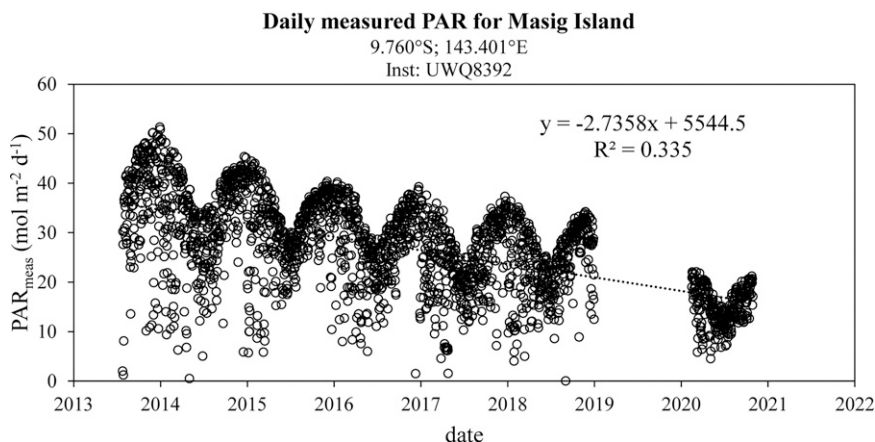


FIG. 6. Trend in daily measured PAR for Masig Island. A linear regression through the data gives a sensitivity loss of $10.1\% \text{ yr}^{-1}$.

TABLE 3. Sensitivity analysis for radiation model using different precipitable water vapor (pww) values and aerosol optical depths (AOD) at 555 nm. PAR_{mod} represents a PAR estimate. Subscripts 99 and 1 refer to the 99th and 1st percentiles, respectively. Columns 4 and 6 represent percentage differences between Ep estimates when compared with Ep using mean values of pww and AOD. Calculations are done for two zenith angles at 0° and 60° . Values are as follows: $pww_{99} = 5.64$ cm; $pww_1 = 1.35$ cm; $\overline{pww} = 3.35$ cm; $AOD_{99} = 0.243$; $AOD_1 = 0.075$; $AOD = 0.159$.

Sequence	PAR	$z = 0^\circ$		$z = 60^\circ$	
		$W\ m^{-2}$	%	$W\ m^{-2}$	%
1	$PAR_{mod}(\overline{pww}_{99}, \overline{AOD})$	553.8	1 vs 5 = 0.3%	240.1	1 vs 5 = 0.4%
2	$PAR_{mod}(\overline{pww}_1, \overline{AOD})$	551.1	2 vs 5 = -0.2%	238.2	2 vs 5 = -0.3%
3	$PAR_{mod}(\overline{pww}, AOD_{99})$	542.5	3 vs 5 = 1.7%	229.1	3 vs 5 = 4.1%
4	$PAR_{mod}(\overline{pww}, AOD_1)$	561.7	4 vs 5 = -1.8%	249.1	4 vs 5 = -4.3%
5	$PAR_{mod}(\overline{pww}, \overline{AOD})$	552.1	—	239.0	—

There is very little sensitivity to water vapor as expected as the PAR region does not cover the infrared water vapor bands (Iqbal 1983). Absolute differences are less than 0.5% in model output when pww averages are used versus the two extremes. This feature appears at both $z = 0^\circ$ and $z = 60^\circ$. Higher sensitivities are obtained for AOD when averages are compared against the two extremes. Absolute values are under 2% at $z = 0^\circ$ and under 5% at $z = 60^\circ$. In the absence of detailed data at each site, “rural” values of $pww = 3.35$ cm and $AOD = 0.159$ have been used for all model runs. A constant factor of $4.57\ \mu\text{mol}\ m^{-2}\ s^{-1}\ (W\ m^{-2})^{-1}$ has been used to convert from watts per square meter to quantum irradiance in the photosynthetically active region (appendix). The conversion factor was estimated for a range of z , τ_{aer} , and pww, with resultant differences in the conversion factor of at most $\pm 0.2\%$ from the above value. A least squares polynomial approximation to the model PAR using solar zenith angles gave the following:

$$PAR_{mod} = -7.1165 + 768.8941cz + 4023.1678cz^2 - 4180.1969cz^3 + 1575.0067cz^4;$$

$$R^2 = 0.999; \text{rms error} = 3.2\ \mu\text{mol}\ m^{-2}\ s^{-1}; n = 21, \quad (4)$$

where “cz” is cosine of the zenith angle and PAR_{mod} are in units of $\mu\text{mol}\ m^{-2}\ s^{-1}$. Equation (4) assumes a mean sun–Earth distance of 1. A correction factor is used for days with sun–Earth distances greater or less than 1 (Iqbal 1983).

The model relationship described in Eq. (4) was evaluated using two high-quality experimental data in the region. The first consisted of 1-min averages from a Kipp and Zonen CM-11 Moll-Gorzyński pyranometer measuring broadband solar irradiance at Townsville Airport (19.248°S, 146.766°E). This high-quality secondary standard instrument (ISO 2018), forms part of the Australian Bureau of Meteorology network and is subject to data reduction and maintenance protocols following the Global Climate Observing System and Baseline Surface Radiation Network (GCOS/BSRN). Calibrations performed at 6-monthly intervals following the alternate method (Forgan 1996) are within than the recommended uncertainty of 3%.

Images for 2017 were scanned for cloudless days using a once-daily satellite view from EOSDIS worldview (<https://worldview.earthdata.nasa.gov>). Data from the selected days

were graphically displayed as line traces and checked for smoothness and regularity. This procedure permitted the selection of 12 days covering 9 months that were cloudless, therefore ensuring a range of climate conditions in the dataset. As no measured PAR data were available at Townsville, the Libradtran model was developed to convert measured broadband solar radiation (E_{BB} in $W\ m^{-2}$) to PAR (in $\mu\text{mol}\ m^{-2}\ s^{-1}$). A constant factor of 4.57 transforms the data from energy units to quantum units as discussed above. The transformation equation included both solar zenith angle and pww obtained as monthly averages, this last variable being necessary given the strong water vapor absorption in the near-infrared bands (Iqbal 1983). The parameterization used similar aerosol conditions as in the estimate of PAR along with solar zenith angle (0° – 85°) and pww of 1, 10, 20, 30, 40, and 50 cm. Parameterization for PAR_{mod} ($\mu\text{mol}\ m^{-2}\ s^{-1}$) is shown in Eq. (5):

$$PAR_{mod} = -23.0055 + 0.4649E_{BB} + 10.1637pww - 0.8229pww^2;$$

$$R^2 = 0.995; \text{RMS error} = 3.3\ \mu\text{mol}\ m^{-2}\ s^{-1}; n = 90. \quad (5)$$

Comparisons between measured and modeled 1-min PAR at Townsville Airport are shown in Fig. 7a. The two datasets are highly correlated with a coefficient of variance greater than 0.998 and an RMS (measured minus model) of $49\ \mu\text{mol}\ m^{-2}\ s^{-1}$, or 3.9% of the measured average. Figure 7b shows how the ratio PAR_{mod}/PAR_{meas} varies with solar zenith angle. These have been obtained by averaging over 5° zenith angle intervals. The ratio is expected to be 1 for a perfect agreement between model and instrument. Part of the error will be introduced by the cosine response of the instrument. Ratios are less than 1, but above 0.95 until around 70° zenith angle.

A second comparison has been done against a Satlantic Hypercor spectral radiometer operating at Lucinda Jetty Coastal Observatory (LJCO; 18.522°S, 146.386°E). The instrument, maintained and operated by CSIRO (www.ermt.csiro.au/html/ljco.html and www.seabird.com/hyperspectral-radiometers) consists of a holographic blazed diffraction grating that spreads the incident light into a linear diode array. The signal at each diode is integrated as a function of time, therefore establishing the signal strength. Spectral irradiance calibration is provided by the

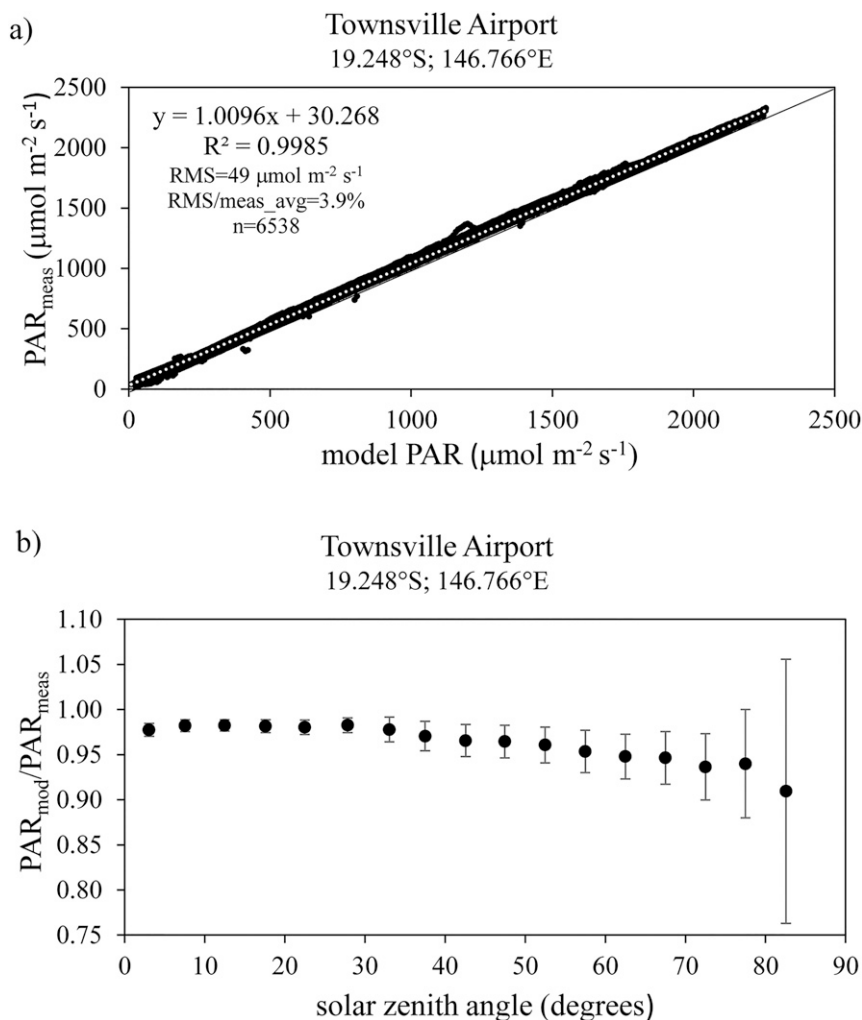


FIG. 7. (a) Measured 1-min PAR data for Townsville Airport vs modeled PAR for the same time interval. Data are based on 12 cloudless days during 2017. Broadband measured data for Townsville has been converted to PAR using a modeled transformation based on Libradtran 1.7. (b) Ratio of modeled to measured PAR vs solar zenith angle for all 1-min data. Data have been grouped according to 5° intervals and averaged. Also shown are the standard deviation of the ratios at these intervals.

factory based on a tungsten-halogen 1000-W lamp that has a calibration traceable to the U.S. National Institute of Standards (NIST) and further validated with in situ laboratory calibrations using Integrated Marine Observing System (IMOS) facilities (Hill et al. 2010). Spectral data are provided at 5-min integration intervals at a spectral resolution of 10 nm.

Fourteen cloudless days were selected for Lucinda Jetty using the same method as in the Townsville comparison. The period extended from August 2015 to June 2016 to match the Lucinda radiometer data stored in the Australian Ocean Data Network (AODN; <https://portal.aodn.org.au/>). Spectral data were integrated at 5-min intervals in the range 400–700 nm to arrive at irradiance units and changed to quantum units following the above conversion factor. Figure 8a shows the scatterplot of measured versus modeled PAR using Eq. (4).

Agreement is good with a correlation of 0.998 and an RMS difference of $35.7 \mu\text{mol m}^{-2} \text{s}^{-1}$, or 2.8% uncertainty of the mean value. Ratios of average model to average measured PAR grouped in 5° bins are shown in Fig. 8b. The ratios are close to 1 with a scatter of ± 0.02 from 0° to 60° , which is in agreement with the cosine errors from the manufacturer. The error increases in the interval 60° – 82° but is still under the cosine error of 10% listed by the manufacturer in this interval (www.seabird.com/hyperspectral-radiometers).

c. Applying the technique for continuous PAR data

Having developed a cloudless-sky PAR model, a series of steps need to be applied to manage the raw PAR and perform the correction as described in Eq. (3). These are shown in Fig. 9. First, a zenith angle corresponding to the midpoint of a

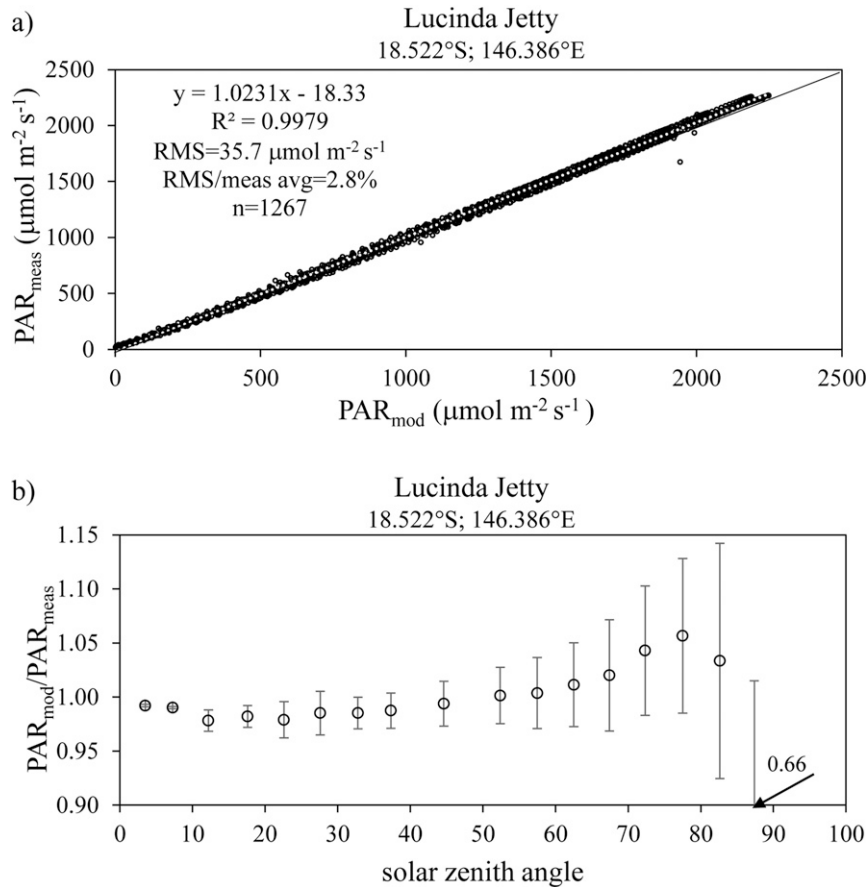


FIG. 8. (a) Measured 1-min PAR data for Lucinda Jetty vs modeled PAR for the same time interval. Data are based on 15 cloudless half days encompassing August 2015–June 2016. Data at Lucinda Jetty represent 5-min averages. (b) Ratio of modeled to measured PAR vs solar zenith angle for all 5-min average data. Data have been grouped in 5° intervals and averaged. Also shown are the standard deviation of the ratios at these intervals. A total of 1267 data pairs have been used in the analysis.

10-min period is estimated. Knowing the zenith angle, a corresponding cloudless PAR is estimated. The next step involves estimating cloudless days. Noontime ratios $c1(d)$ (model/measured) are extracted for cloudless days and applied to all data using an interpolation scheme. The zenith angle correction $c2(z)$ is then obtained for cloudless days once the noontime corrections are available. The final corrected value PAR_{corr} is given as the product $c1(d) \times c2(z) \times \text{PAR}_{\text{raw}}$, which is shown in Fig. 9.

The next sections describe each of these steps in more detail using data collected at Cape Bowling Green (19.305°S, 147.393°E).

1) EXTRACTING CLOUDLESS DAYS

Separating cloudless from cloudy episodes is labor-intensive. Recent approaches deal with extracting cloudless periods from a time series of global, direct and diffuse irradiance from well calibrated broadband instruments (Perez et al. 1987; Long and Ackerman 2000; Reno and Hansen 2016; Gueymard et al. 2019). Most of the techniques partition the global irradiance into direct and/or diffuse irradiance to develop clearness indices according to various criteria. Our requirements are not similar as

our data are not calibrated, and in addition, there is no diffuse irradiance measured. However, Reno and Hansen (2016) applied a series of criteria based on similarity between measured and cloudless modeled irradiance to extract cloudless conditions. The technique was robust and compared well with other methods. We have adopted a modified form of this approach as shown below.

For every day of record a cloudless irradiance is produced and compared with measured PAR at 10-min averaging intervals (Fig. 10). Modeled cloudless irradiance (PAR_{mod}) is multiplied by a constant factor (F) of 2.0 and then lowered in steps of 0.1 (2.0, 1.9, ..., 1.0, ..., 0.2). Measured and modeled irradiance are compared at every step F using a normalized standard deviation as shown in Eq. (6):

$$\text{DIFF}_F = \frac{\left[\frac{\sum_{i=1}^N (\text{PAR}_{\text{mod}_i} - F \times \text{PAR}_{\text{meas}_i})^2}{N} \right]^{1/2}}{\left[\frac{\sum_{i=1}^N \text{PAR}_{\text{mod}_i}}{N} \right]} \times 100, \quad (6)$$

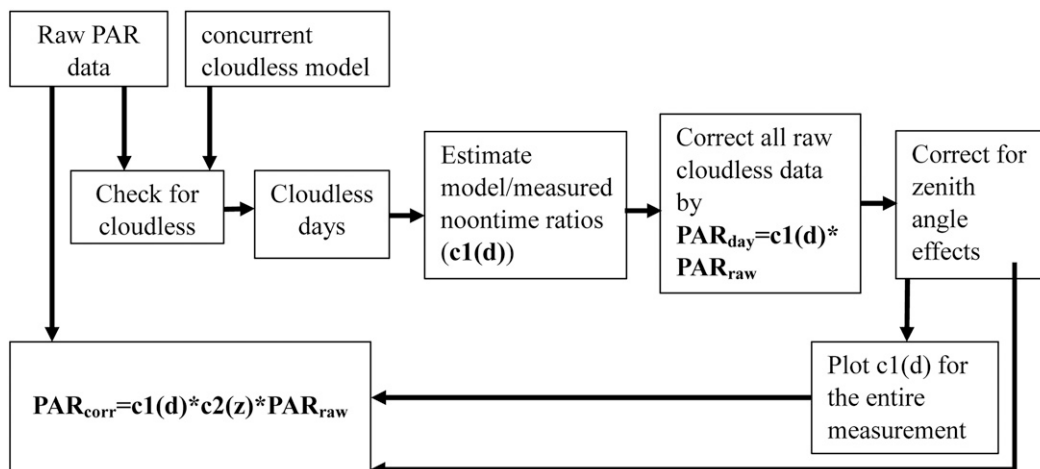


FIG. 9. Flow diagram describing details of the correction procedure.

where PAR_{measi} and PAR_{modi} are measured and modeled 10-min irradiances (i) and $DIFF_F$ is an index of deviation applied over the entire day ($i = N$) and expressed in percentages. Cloudless days will have a low $DIFF$ value approaching 10% or lower for a particular value of F . No value of F will provide a low $DIFF$ in cloudy days by virtue of the variability in PAR . Additionally, a value of F expresses the constant factor by which the raw PAR has decreased or increased throughout the day.

Figure 11 (right axis) shows the factor F for the deployment period of instrument UWQ99287 at Cape Bowling Green. It

was deployed on 19 November 2015 and picked up on 6 November 2017. A threshold of 5% or less was used for $DIFF$ to detect cloudy days, giving 95 cloudless days for the 2-yr period. These were then checked by examining the visual trace for smoothness. Cloudless conditions are detected immediately upon deployment, on day 0, with an F factor of 0.9. This F factor remained constant until day 127 when it went to 0.8 and going down again to 0.7 on day 327. The lowering of F relates to a decreasing instrument sensitivity when recording cloudless days.

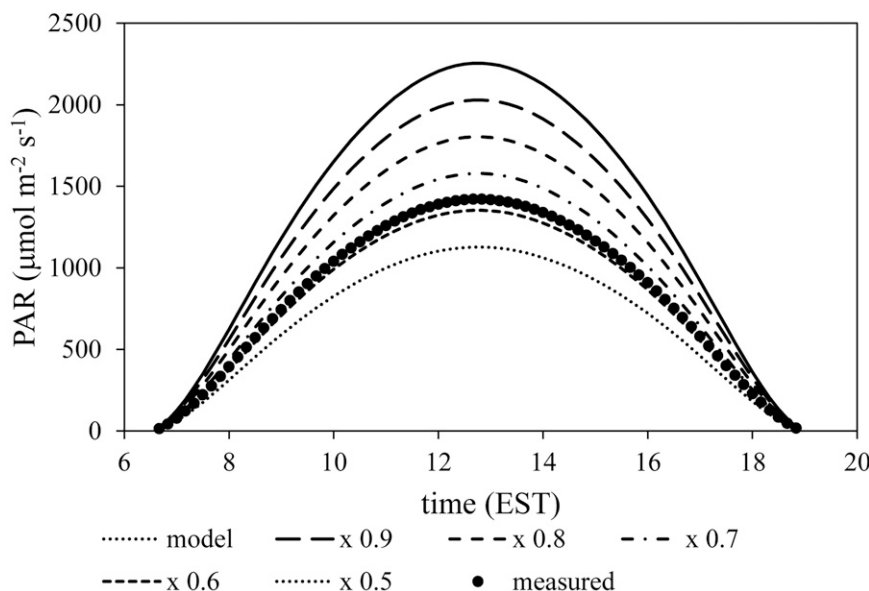


FIG. 10. Cloudless-day detection. Model irradiance (heavy line) is diminished by a constant factor in steps of 0.1. At each step the standard deviation between measured and modeled values are estimated for all 10-min data. A cloudless day will be accepted if it is below a certain standard deviation threshold. In the above example, a cloudless day meets the criterion when multiplying all modeled data by 0.6.

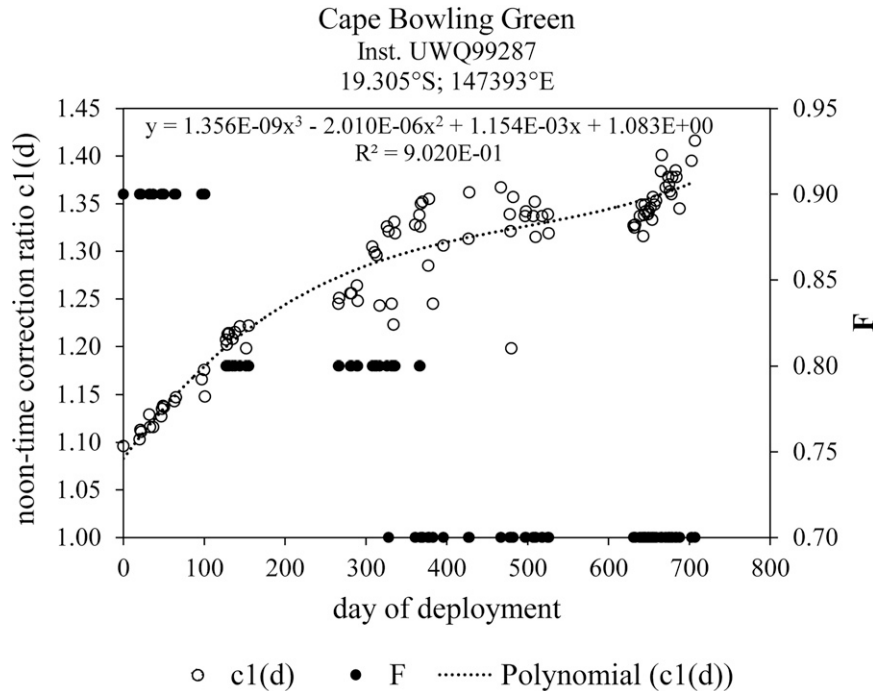


FIG. 11. Plot of $c1(d)$ vs day after deployment d (left y axis). Plot of daily correction factor F vs day after deployment d (right y axis). Instrument UWQ99287 was deployed on 19 Nov 2015 and picked up on 6 Nov 2017.

2) ESTIMATING NOONTIME CORRECTION RATIOS

For each cloudless day a noontime correction ratio $c1(d)$ is applied, Eq. (3b), and these are plotted on the left Y axis of Fig. 11. They trace a smooth nonlinear curve that increases in time as the instrument decreases in sensitivity. A cubic polynomial fit to the data gives

$$c1(d) = 1.356 \times 10^{-9} d^3 - 2.010 \times 10^{-6} d^2 + 1.154 \times 10^{-3} d + 1.083;$$

$$R^2 = 0.902, \text{RMS}(X_i - Y_i) = 0.027, \quad (7)$$

where d is day after deployment. The above expression is applied to all days of the deployment period, is taken as constant during the day, and is used to correct for all 10-min irradiance data PAR_{raw} as in Eq. (3a).

3) ESTIMATING ZENITH ANGLE CORRECTION RATIOS

Applying $c1$ to all 10-min data will account for seasonal degradation, but diurnal discrepancies caused by cosine errors could still appear in the data. To account for this effect a second correction $c2(z)$ is applied, which is the instantaneous ratio of model PAR (PAR_{mod}) to the measured (PAR_{raw}) corrected for seasonal degradation ($c1 \times \text{PAR}_{\text{raw}}$) as shown in Eq. (3a). In ideal conditions $c2(z)$ will equal 1 with perfect cosine response and no tilt in the platform. We examine this effect in two stages: first, by using a modeled virtual instrument that uses the cosine responses of the four Licor sensors

listed in Fig. 3; and second, by examining errors introduced by tilting of the instrument platform.

Cosine responses shown in Fig. 3 were modified for the analysis. Each response estimated over incidence angles $+90^\circ$ to -90° were changed to two responses, covering 0° to $+90^\circ$ and assumed to be representative of two different instruments. This step is suitable for the analysis, which is concerned with typical errors introduced by the cosine responses. As a result, a total of eight cosine responses were available for the virtual instrument.

The Libradtran model was executed with the same input conditions as already described in section 2b. Direct and diffuse PAR irradiance was estimated at 5° zenith angle intervals from 0° to 85° . This dataset was used with a virtual instrument using the eight different cosine responses. As a first step diffuse irradiance from Libradtran is compared with the virtual instrument using a specific cosine response. An approximate ratio (C_θ) between the two diffuse irradiances may be obtained by assuming isotropic radiance (R) from the sky:

$$C_\theta \left[2\pi R \int_{\theta=0}^{\theta=90} \sin\theta \cos\theta \, d\theta \right] = 2\pi R \int_{\theta=0}^{\theta=90} \sin\theta f(\theta) d\theta, \quad (8)$$

$$C_\theta E_{\text{DIFFM}} = E_{\text{DIFFI}}$$

where the left-hand side of Eq. (8) is a cloudless-sky model diffuse irradiance (E_{DIFFM}) and the right-hand side represents the equivalent instrument measurement with its own cosine

TABLE 4. Comparison of global PAR irradiance using a virtual instrument with Libradtran 2.0.4 estimates. Each row corresponds to a different cosine response curve covering a solar zenith angle range from 0° to 85° in steps of 5° . RMS represent the RMS difference between the model with and without a specific cosine response. The last column represents the uncertainty (%) when normalized by the mean global radiation E_{GLM} ($=294.5 \text{ W m}^{-2}$).

Instrument	Cosine response range	RMS difference (W m^{-2})	$100 \times \text{RMS}/E_{GLM}$ (%)
7157	0 to $+90$	2.10	0.71
7157	0 to -90	6.09	2.07
7830	0 to $+90$	4.37	1.49
7830	0 to -90	2.16	0.73
8957	0 to $+90$	2.60	0.88
8957	0 to -90	4.38	1.49
10045	0 to $+90$	6.59	2.23
10045	0 to -90	3.35	1.13
Average		3.95	1.3

response (E_{DIFFI}). The virtual instrument global irradiance may then be described as

$$E_{GLI}(z) = E_{DIRI}(z) + E_{DIFFI}(z) \quad (9a)$$

$$= E_{DIRM}(z)f(z) + C_\theta E_{DIFFM}(z), \quad (9b)$$

and subscripts DIR, DIFF, and GL stand for direct, diffuse, and global, respectively, while I and M represent instrument and model.

Global irradiances for the PAR region were compared using model output [$E_{GLM}(z) = E_{DIRM}(z) + E_{DIFFM}(z)$] with its virtual instrument irradiance $E_{GLI}(z)$ using Eq. (9b). Comparisons were done for 18 solar zenith angle intervals of 5°

and eight different instrument cosine responses. Root-mean-square differences are presented in Table 4. Differences are small, covering a range between 2.10 and 6.59 W m^{-2} . These translate to percentage differences between 0.71% and 2.23% of the mean model irradiance of 294.5 W m^{-2} . Figure 12 shows average differences between global irradiance from the model and eight estimates from the virtual instruments as a function of solar zenith angle. Averages are estimated over absolute values and they show that differences are under 5% up to a zenith angle of 80° . Based on these results, it is unlikely that instrument cosine responses is an important factor in increasing the overall instrument uncertainty.

The platform stability, however, could present more serious problems. Instruments based on poles or similar platforms are not mounted on gimbals and these could shift over time due to wave action, strong currents, or soil movement. At present there is no method to assess how horizontal the sensor surface was when examining historical data. However, a sensitivity test may be performed to assess the likely errors associated with tilting of the platform. As in the previous section the Libradtran model was used to estimate direct and diffuse PAR irradiance. Data for 21 December were chosen as they correspond to the Southern Hemisphere summer solstice with high irradiance levels. Coordinates for Myrmidon Reef were used along with a range of cloud conditions and two tilt angles, 5° and 15° . Table 5 gives details of the model inputs.

A sensing surface was designed with a tilt angle α to the vertical and at some azimuth angle ω to the local south (Fig. 13). The global PAR irradiance received by the tilted plane may be written as (Iqbal 1983)

$$E_{GLI} = E_{DIRM} \times \cos(\theta_{INC}) + E_{DIFFM} \times (1 - \text{GVF}) + E_{GLM} \times 0.05 \times \text{GVF}. \quad (10)$$

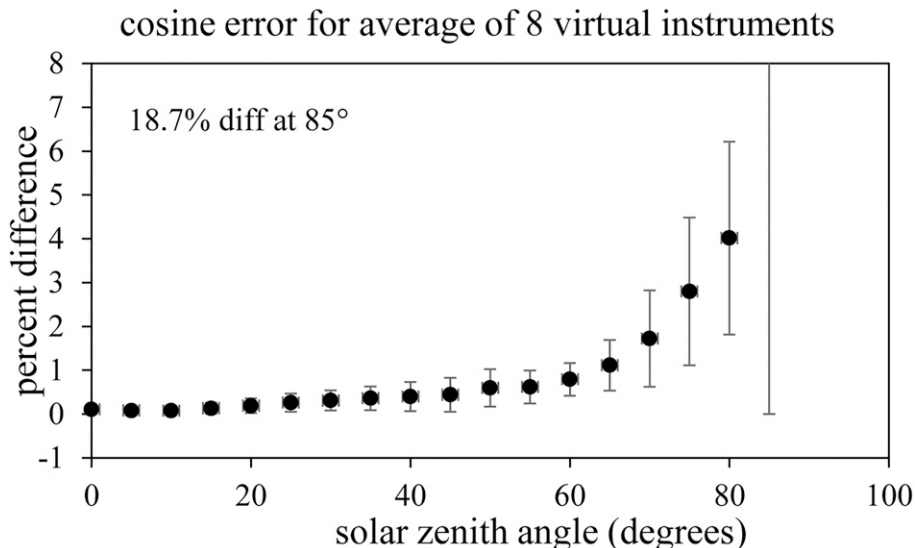


FIG. 12. Average of absolute differences between global irradiance from model minus global irradiance from eight virtual instrument. Percentage differences are referenced to model global irradiance at a particular zenith angle.

TABLE 5. Libradtran model input for platform tilt analysis.

Date	21 Dec
Location	Myrmidon Reef: 18.274°S, 147.382°E
Output	Direct PAR irradiance, diffuse PAR irradiance, zenith angle, solar azimuth angle
Frequency of output	Every 15 min
Sky conditions	Cloudless, 3/10 cloud cover, 7/10 cloud cover, 10/10 cloud cover
Cloud optical depth	Liquid water cloud of optical depth 10
Cloud-base height	2-km base height and 2-km thickness
Tilt angle	15°, 5°
Aspect	30° clockwise from north

The first term on the right of Eq. (10) describes the direct beam irradiance incident on the tilted plane with incidence angle θ_{INC} . Diffuse irradiance received from the sensing surface will depend on the ground view factor GVF, which is the fraction of the irradiance on the sensor from the water surface assuming equal and isotropic irradiance from the sky and water (Iqbal 1983). It may be written as

$$\text{GVF} = \frac{1}{2}[1 - \cos(\alpha)]. \quad (11)$$

Using this relationship, the second term on the right describes the diffuse irradiance on the sensor from the sky, while the last term is the irradiance from the sky after reflection by the water surface. All terms in Eq. (10) may be readily obtained with the exception of θ_{INC} , which may be estimated in terms of the direction cosines of the direct beam and the normal N to the tilted surface in Fig. 13 (Arfken et al. 2005).

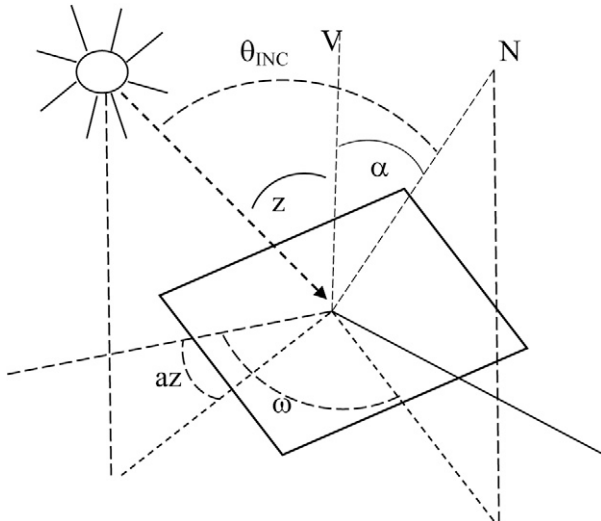


FIG. 13. Geometry for solar radiation incident on an inclined plane. Direct radiation from the sun subtends a zenith angle z with respect to the local vertical V and an azimuth angle az with a reference line, typically north. The tilted plane is characterized by a tilt angle α and azimuth angle ω with respect to south. Direct irradiance on the tilted plane is determined by θ_{INC} , the angle between the direct beam and N .

Equation (10) was used to estimate E_{GLI} for all conditions described in Table 5. Percentage difference between horizontal irradiance [$E_{\text{GLM}} = E_{\text{DIRM}} \times \cos(z) + E_{\text{DIFF}}$] and sensor irradiance (E_{GLI}) was estimated at each 15-min time step. Figure 14 presents results for two different tilt angles. Several features are noticeable in the two diagrams. Positive differences appear in the morning while negative differences are prominent in the afternoon, a result of the northeasterly aspect of the surface resulting in low θ_{INC} . Percentage differences in both figures are minimized by cloud cover. For example, a cloud cover of 3/10 will reduce differences by 20%–25% while 7/10 coverage will bring differences down by approximately 50%. Differences go down markedly with lower tilt angle. At 1500 EST they are -11.7% for clear skies and 15° tilt (Fig. 14a) but are much lower at -4.4% for a tilt angle of 5° (Fig. 14b).

Estimating uncertainties due to sensor inclination is difficult as there is an added dependence on cloud cover. However, positive differences appear to be at or below 5% but negative differences are much higher in absolute magnitude when θ_{INC} is large, which produce low direct irradiances. These results argue for the need to keep the sensing surface as horizontal as possible and if achievable, under 10° tilt angle.

Given the satisfactory performance of the cosine response, the second correction $c_2(z)$ was taken as 1.0 indicating no change in the raw signal due to diurnal changes in solar zenith angle z . The assumption is made that changes in platform inclination are small, and in most cases will introduce irradiance differences of under 5%. As a result, Eq. (3a) may be written as

$$\text{PAR}_{\text{corr}}(d, z) = \text{PAR}_{\text{raw}}(d, z) \times c_1(d). \quad (12)$$

4) UNCERTAINTY ANALYSIS

It is possible to provide an estimate of the total uncertainty in $\text{PAR}_{\text{corr}}(d, z)$ of Eq. (12). The noontime ratio $c_1(d)$ has an uncertainty related to a least squares fit of the seasonal trend. Similarly, PAR_{raw} is an approximation as there are uncertainties associated with responses of the instrument due to instrumental cosine errors or changes in the platform inclination. For purposes of the uncertainty analysis, it is convenient to define PAR_{corr} as being dependent on two parameters:

$$\text{PAR}_{\text{corr}} = [\text{PAR}_{\text{raw}} \pm 4\%] \times c_1(d), \quad (13)$$

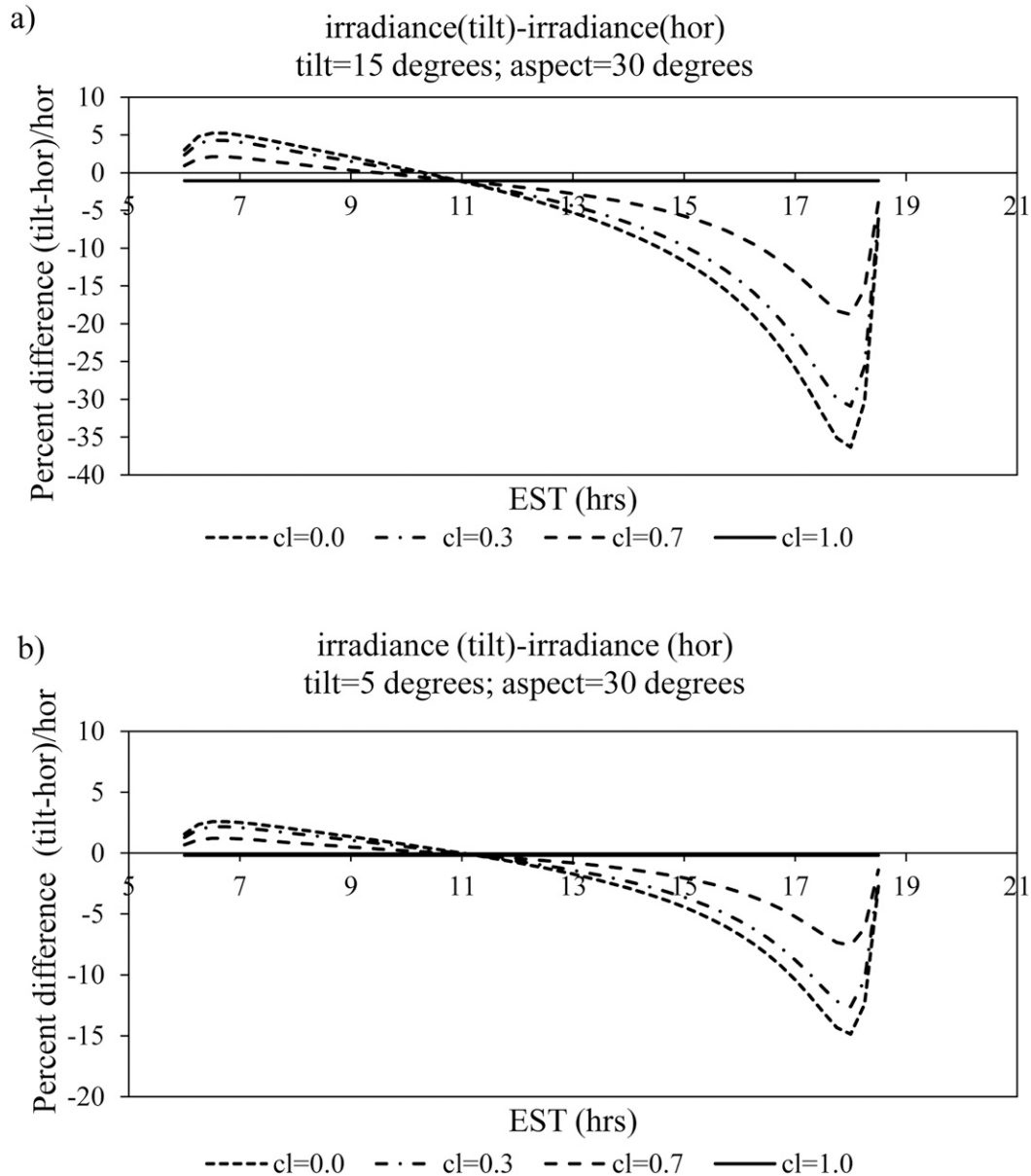


FIG. 14. Percentage difference between inclined and horizontal irradiance for (a) a tilt angle of 15° and (b) a tilt angle of 5°. In both cases the surface has an aspect of 30° from north.

where the uncertainty in PAR_{raw} arises from inherent instrument errors such as cosine responses, temperature responses, or platform misalignments. In the previous section we showed that cosine response uncertainties were small, averaging less than 2% but errors due to platform alignments were larger. In the absence of detailed platform data, we have chosen the uncertainty in PAR_{raw} as 4%, a daily average for a platform having a tilt of 5° and facing NE. Using propagation of error analysis (Young 1962), we can derive an uncertainty in PAR_{corr} :

$$\begin{aligned} \delta PAR_{corr} &= \frac{\partial PAR_{corr}}{\partial c1} \delta c1 + \frac{\partial PAR_{corr}}{\partial PAR_{raw}} \delta PAR_{raw} \\ &= PAR_{raw} \delta c1 + c1 \delta PAR_{raw}, \end{aligned} \quad (14)$$

and δPAR_{raw} is simply $0.04 \delta PAR_{raw}$. However, $\delta c1$ will depend on the characteristics of the trend as will be discussed in the validation section.

5) TRENDS IN RAW VERSUS MEASURED DAILY IRRADIANCE

Raw 10-min PAR data may now be corrected as in Eq. (3a) once the functions for $c1$ are determined. As already discussed, $c1$ is applied to all-sky conditions. In the case that the first cloudless day ($d0$) occurs after deployment, $c1(d)$ is taken as equal to $c1(d0)$ for all days before $d0$. If instrument pickup occurs after the last cloudless day dn , $c1(d) = c1(dn)$ for all days after dn .

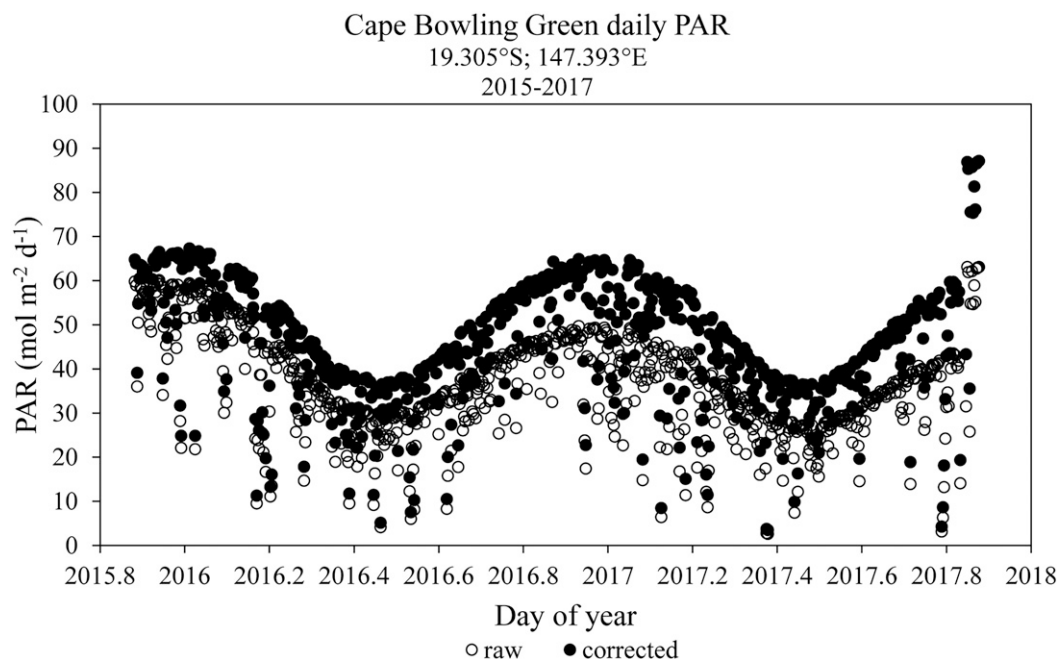


FIG. 15. Daily PAR for uncorrected (open circles) and corrected PAR (closed circles) for Cape Bowling Green. Total deployment period was from 19 Nov 2015 to 6 Nov 2017.

Figure 15 shows the daily pattern for corrected and raw PAR for the duration of the deployment period of instrument UWQ4917 at Cape Bowling Green, a period of 732 days. Daily differences between the two datasets increase over time. Upon deployment daily differences are 7.7% with the corrected PAR being slightly higher. Just before pickup these differences have increased to 27.6%.

4. Instrument intercomparison

All instruments are sent to the factory after the field season where they are recalibrated with a quartz-halogen lamp traceable to NIST. An indication of degradation could be performed by comparison of the multiplier constant before and after recalibration. However, a proper assessment of the

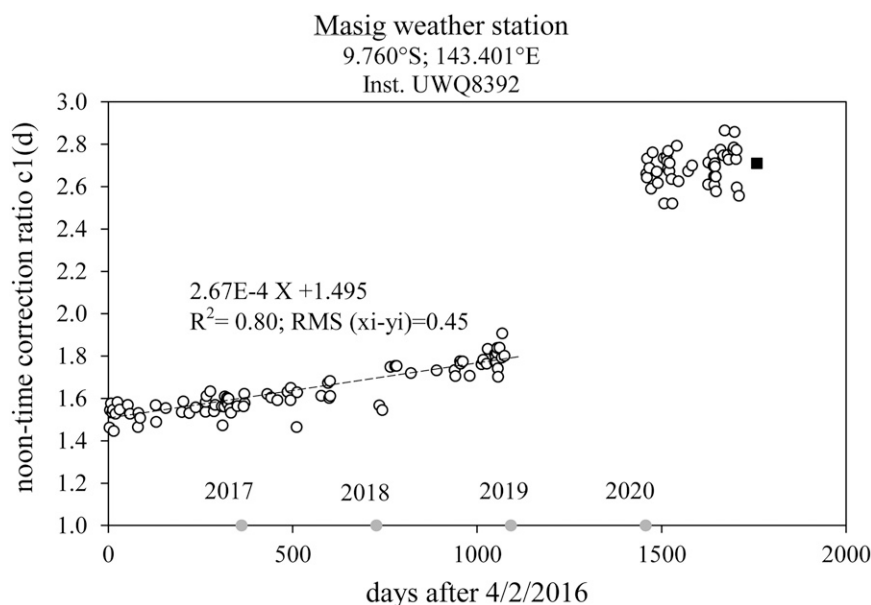


FIG. 16. Noon-time correction ratios for Masig Island. The black square on the far right represents date of instrument comparison.

technique must involve simultaneous comparison of PAR_{corr} with in situ independent measurements of PAR. The reason is that the correction factors applied in this study are not only dependent on the changing properties of the instrument, but on deployment characteristics such as local obstructions, instrument leveling, and instrument wiring. Furthermore, instrument sensors are cleaned at the factory, which might change the optical properties of the diffuser and further complicate the task of correcting the recorded data.

Two field comparisons have been performed here. They involve independent measurements using an MS9 multispectral sensor from In-situ Marine Optics (<http://insitumarineoptics.com/ms9/>). The instrument records incoming spectral solar irradiance in nine distinct silicon photodiode channels covering the ultraviolet and visible bands (364.0, 385.3, 439.9, 491.1, 548.6, 589.6, 635.4, 658.4, and 700.9 nm). Each channel records irradiance with a 10 nm full width half maximum. Irradiance cosine response is less than 3% uncertainty from 0° to 60° incidence angle. Calibration is obtained by comparison with an NIST traceable quartz-halogen lamp. In burst mode, data are acquired at 10 Hz, and stored in memory every second. All spectral data were averaged over 10-min periods to coincide with Licor PAR data and integrated from 400 to 700 nm using trapezoidal integration.

It must be emphasized, however, that comparison with an accurate spectrometer with an NIST-traced calibration serves as a validation of the technique and is not meant to provide an absolute calibration. Even if agreement between the two radiometers (the MS9 and the corrected Licor) is very high with a correlation coefficient approaching one, the Licor instrument is still limited by its inherent uncertainty of $\pm 4\%$ – 5% .

a. Masig Island comparison

The weather station housing the Licor 192 quantum sensor is located in Torres Strait (9.760°S , 143.401°E) and approximately 53 km from mainland Papua New Guinea. All instruments rest on a 6 m galvanized steel pole of 20 cm diameter anchored to a reef just off Masig Island and approximately 6 m from the mean water level. The Licor was deployed in June 2013 but was not replaced given the remoteness of the location and difficulties in accessing the site by the AIMS research vessel. The site comes under the jurisdiction of the Torres Strait Regional Authority, who maintains the site with occasional visits.

Data from the instrument were compared with the MS9 multispectral radiometer on 28 October 2020 and subsequently the instrument was replaced. Figure 16 shows a plot of the daily noontime correction ratio from 4 February 2016 until the day of the radiometer intercomparison. There is a gradual increase in $c1(d)$ from 1.5 on 4 February 2016 to 1.8 on the 9 December 2018. The data acquisition ceased after this date due to problems with the 3G communication and malfunction of the replacement 4G communication. It was only on 4 January 2020 that data acquisition became operational again. Correction ratios were significantly higher during the rest of 2020 until the date of the intercomparison. Furthermore, no significant trend in time was found in $c1(d)$ and for

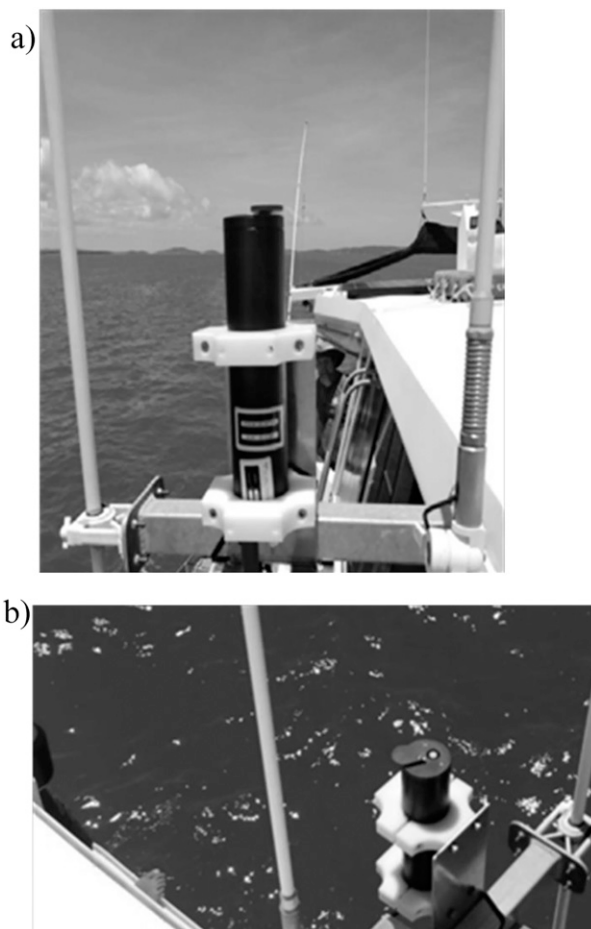


FIG. 17. MS9 spectral radiometer deployment aboard the top deck of the M/V *Free Spirit*. (a) Side view; (b) top view.

purposes of the instrument comparison an average value was used for 2020: 2.69 ± 0.08 .

A charter vessel, the M/V *Free Spirit* was used for the intercomparison and instrument replacement. It is a 14.98 m long catamaran with an upper deck providing a fixed platform allowing good sky views free of local obstructions. Figure 17 shows the MS9 deployment on the top deck with a side view (Fig. 17a) and top view (Fig. 17b). Upon arrival at the tower site the vessel was anchored next to the tower at a distance of approximately 50 m, ensuring that both radiometers were sampling the same radiation field but far enough to minimize mutual obstruction from the vessel or tower. Thus, the two radiometers recorded simultaneously at the same site for all the afternoon of 28 October 2020. The sensor level was checked the following day using visual and digital photographs. These gave a probable sensor offset of under 5° from the horizontal.

Figure 18 plots 10-min averages of both instruments. There is a coefficient of variance of 0.99 between corrected Licor data and the MS9, with the slope of the two datasets within one standard deviation of the 1:1 line (slope = 0.940; intercept = $10.572 \mu\text{mol m}^{-2} \text{s}^{-1}$). Also shown are the error bars using

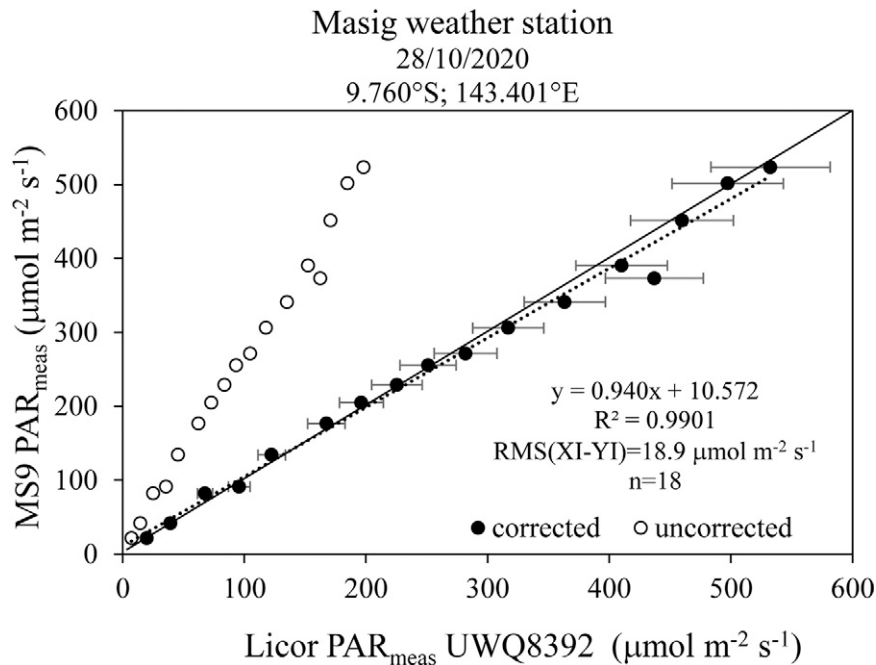


FIG. 18. Plot of 10-min averages of PAR estimates from instrument UWQ8392 against the MS9 PAR. Filled circles are corrected Licor PAR estimates; open circles are uncorrected.

Eq. (15) with a daily correction uncertainty ($\delta c1$) of 0.08. Individual estimates from the Licor are within one standard deviation of the MS9 estimates in 16 out of the 18 data points (Fig. 18). Also shown are the uncorrected data as open circles, which feature a larger slope with respect to the MS9 ($\text{MS9} = 2.528\text{Licor} + 10.572$).

b. Myrmidon Reef comparison

The weather station is located in the central part of the GBR with latitude and longitude coordinates of 18.274°S, 147.382°E (Fig. 1). The instruments rest on a 12-m galvanized steel tower at 10 m above mean sea level (MSL). Instruments were interchanged on 11 March 2021 and at that time the existing instrument, a Licor UWQ9529 was replaced for a fresh recently calibrated instrument. This visit using the AIMS research vessel Solander provided an opportunity to compare the UWQ9529 signal with the MS9 spectrophotometer carried on the vessel. The Licor UWQ9529 was deployed on 3 July 2019 and it is possible to examine daily noontime correction ratios from that date onward (Fig. 19). Also shown are ratios for the previous instrument (UWQ99276) deployed at the station, from 27 July 2017 to 3 July 2019. Trends in the ratios are affected by outliers caused by cloudy periods and to remove them a threshold of two standard deviations from the regression line was used. This threshold was successively applied until no outliers appeared in the two trends. This filter essentially removed 10 and 5 days from the record of UWQ99276 and UWQ9529, respectively.

Figures 19a and 19b show a plot of $c1$ with and without outliers removed, respectively. Trends for the two instruments differ markedly, with instrument UWQ99276 showing increasing

$c1$ with days after deployment, approximately 0.144 yr^{-1} or 28.8% after a 2-yr recording episode. By contrast, there is very little evidence of change in the ratios for UEQ9529 as the slope is not significant. It is interesting to note, however, that the ratio for UEQ9529 averages out at 0.745 ± 0.026 , considerably below unity needed for perfect agreement between measurements and the radiation model.

An instrument comparison was conducted from 1235 EST 9 March until 1405 EST 11 March 2021. Care was taken to ensure that the Licor instrument remained undisturbed in its original position during the experiment. The first task involved visual and photographic checks on the sensor level, which gave an approximate tilt of around 4° . The MS9 was attached in close proximity to the Licor UWQ99276 and both systems continued recording separately (Fig. 20)—the Licor signals were averaged every 10 min and the MS9 recording at 10 Hz and was averaged at 10-min intervals to coincide with the Licor. Both sensors had unobstructed sky views with the exception of a Vaisala Weather Transmitter sensor located at around 1 m from the Licor and MS9 sensors. Sky view factor calculations indicated that the obstruction contributed approximately 0.5% of the total sky hemisphere radiation into both sensors.

Figure 21 plots the two signals for the 3-day measurement period. Integrated PAR irradiance from the MS9 instrument was converted from W m^{-2} into $\mu\text{mol m}^{-2} \text{s}^{-1}$ using a factor of 4.57 (appendix). The raw signals from the Licor sensor were multiplied by a mean correction ratio of 0.745 corresponding to the entire deployment period for the sensor (Fig. 21). There is a high coefficient of variance between the two signals exceeding 0.99 with an RMS difference of

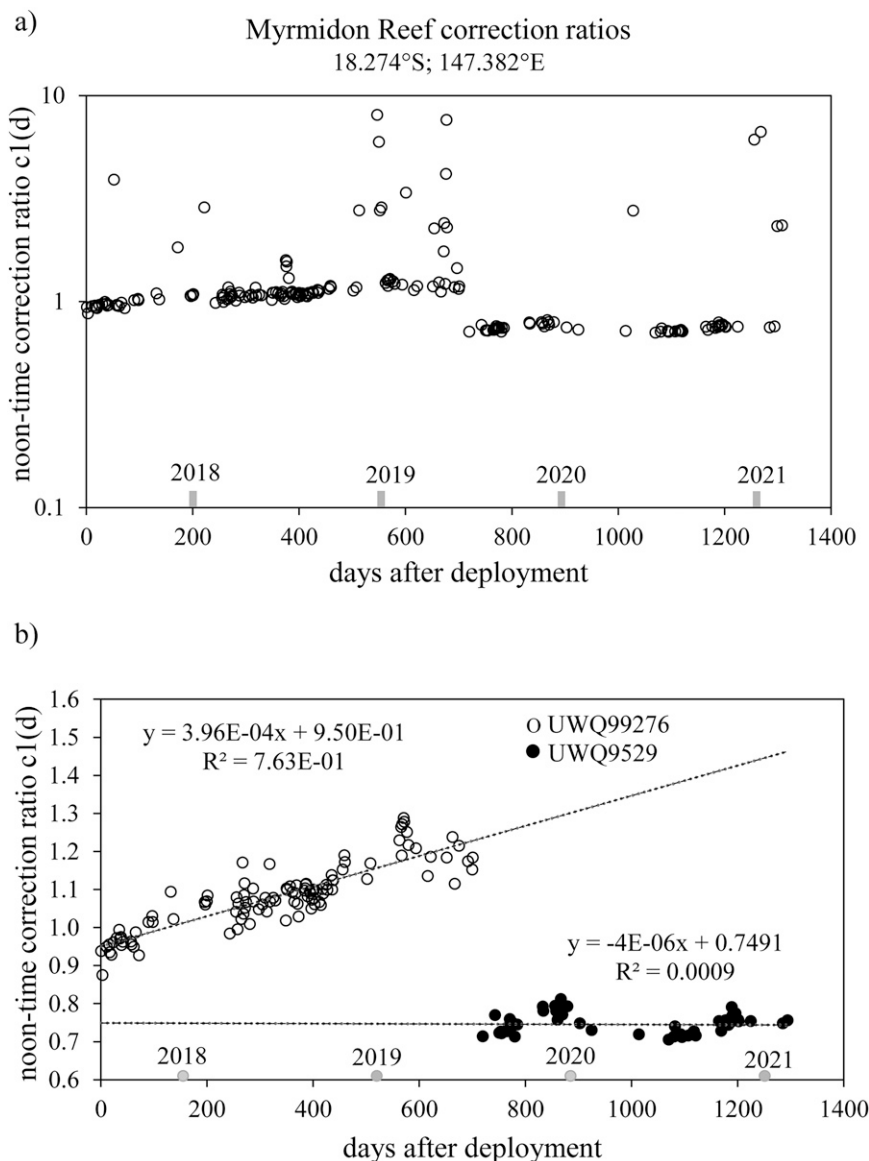


FIG. 19. Plot of correction ratios from day of deployment of UWQ99276, which was on 27 Jul 2017. (a) On a logarithmic plot with all outliers shown. (b) After all outliers have been removed on a linear scale. Instrument UWQ99276 was picked up on 3 Jul 2019 and was replaced by instrument UWQ9529.

$86.3 \mu\text{mol m}^{-2} \text{s}^{-1}$. This figure translates to an uncertainty of 6.7% of the mean PAR measured by the MS9: $1289 \mu\text{mol m}^{-2} \text{s}^{-1}$. There is evidence, however, of a slight hysteresis in the plot, which could be a result of several factors including aerosol changes during the day or tilt error relating to departure of the sensor from a horizontal position.

5. Discussion

Unattended PAR measurements in marine environments are prone to large errors, and in the absence of frequent maintenance and replacement, a cloudless PAR model can provide

a daily view of its performance and response to a range of environmental forcing. Thus, disturbances in sensor performance due to diurnal and seasonal changes in solar zenith angle, wind and temperature, platform shift, and storm systems among others can be examined and assessed insofar as the instrument can replicate a cloudless-sky model. The technique can then provide a convenient quality control mechanism and correction factors to apply while the instrument is deployed between factory calibrations. Comparison of corrected values with a traveling spectrophotometer gave RMS errors of between 6% and 8% of mean measured values, which are slightly higher than the factory-quoted error of 5%.



FIG. 20. Instrument intercomparison at Myrmidon Reef (18.274°S, 147.382°E) conducted from 9 to 11 Mar 2021. (a) Deployment of the MS9 (SN0049) spectrophotometer. (b) the Licor quantum sensor (UWQ99276). All three instruments are separated by a distance of approximately 1 m.

The method relies on the applicability of a cloudless-sky model, which has been validated at two sites in the GBR region. In heavily polluted or heavily urbanized regions it is expected that the model will overpredict clear sky conditions (Bergin et al. 2017; Janjai et al. 2009; Jáuregui and Luyando 1999; Nunez 1993). In the western Pacific oceanic regions, Nunez (1993) found that 4.8% of broadband solar radiation was depleted by aerosols on an annual basis. This figure was obtained from rural pyranometer stations in the region. Daily total depletion by aerosols in the cloudless model described here is 3.1%, which agrees to within 1.7% with data from the pyranometer stations.

Results from this study indicate that signal degradation is considerable and may reach values of over $10\% \text{ yr}^{-1}$. Furthermore, the character of the degradation changes with the instrument and the environment and it is difficult to predict. In some cases it may involve a linear or nonlinear change. Other situations may involve programming errors during deployment and no observable degradation. In any case our technique provides an ongoing check on the behavior of the field instrument and an ability to correct for periods between calibrations.

Although difficult and challenging, PAR measurements from photovoltaic sensors play an important role in supplementing data from other methods. Satellite methods have been used to map PAR solar radiation at a global and regional scale (Frouin et al. 2018; Van Laake and Sanchez-Azofeifa 2005; Frouin and Pinker 1995). There is currently a MODIS product providing daily PAR at 5-km resolution for the entire globe (<https://doi.org/10.5067/MODIS/MCD18A2.006>). However, uncertainties grow rapidly at short temporal scales and most of the current studies restrict themselves to the daily scale at the lower limit. Typically, RMS errors can range from 20% to 35% and higher at the daily scale or less (Frouin and Murakami 2007; Nunez et al. 2005). Within this context Licor PAR data, with an uncertainty of 6%–8%, can play a useful role in assessing the satellite product.

Uncertainties in satellite PAR estimates at short time scales are mainly a result of the considerable spatial and temporal variability in cloud structure and composition, which often involve sub-pixel-scale variability (Nunez et al. 2016, 2005). At the hourly scale these uncertainties could overwhelm satellite studies involving, for example, comparisons between two stations recording PAR. The lower uncertainties related to the Licor sensor would make these instruments a good candidate for examining short-term fluctuations in PAR during cloudy episodes.

Much of the demand for PAR data in the GBR relate to studies involving productivity in subsurface environments. Typically, it might involve two PAR sensors, one above and a second at some specified depth below the surface, designed to estimate PAR depletion in the water column. Many applications need extended PAR records, which require quality controls such as the ones described here (Robson et al. 2020). Satellite data may be used to provide PAR if the experiment extends over weeks or months, but the problem becomes complex if subsurface light is desired and water turbidity changes at high frequencies. In this situation both above and below PAR measurements would be needed to fully understand the light field (Jones et al. 2020).

The experience gained in this study has provided us with a set of guidelines that may be used to monitor, detect, and correct records while the instruments are deployed in the field, and to correct observations post deployments. The work is continuing as there are processes that have not been examined and could still be important in affecting the quality of the signal. Many of the records have a seasonal variability that may relate to wind and temperature effects or seasonality in solar heating of the instruments. Errors in positioning must be studied further as there could be stations with unstable platforms that have slowly shifted in orientation over time. Some of the studies may involve field observations or alternatively laboratory studies.

6. Conclusions

Based on the above study, the following recommendations are outlined for long-term management of photovoltaic sensors that are left unattended in marine environments.

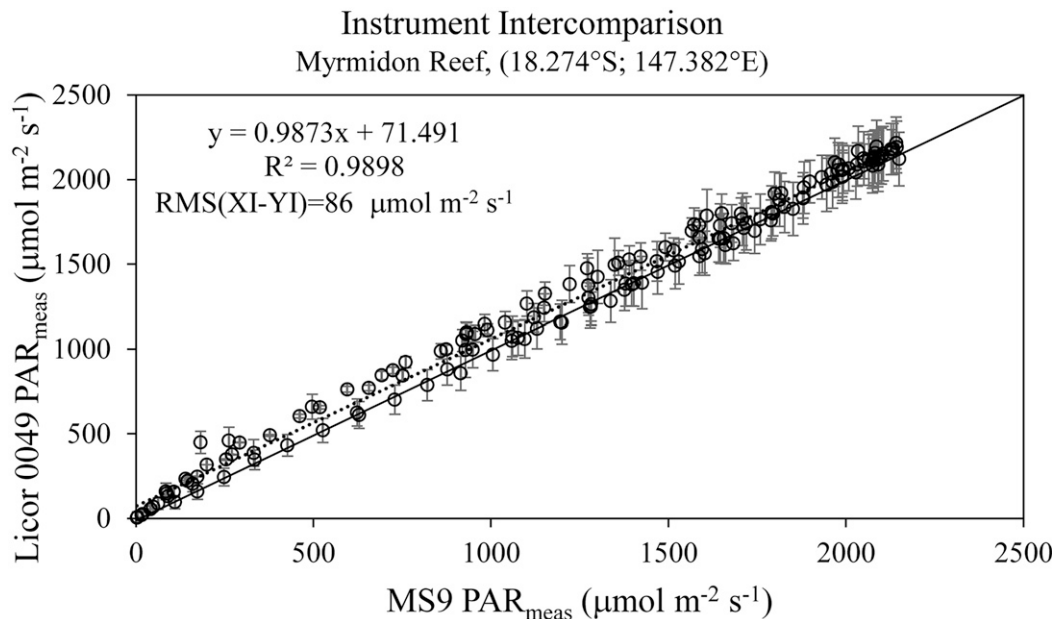


FIG. 21. Plot of PAR from the Licor quantum sensor UWQ9529 vs PAR from the MS9 (SN00949). The 10-min averages are estimated during the period 1235 EST 9 Mar to 1405 EST 11 Mar 2021. Error bars are estimated using Eq. (15).

a. Correcting historical data

This research has shown that degraded observations can be upgraded postdeployment if appropriate corrections can be determined through analysis of cloud-free days during deployment. This is a critical outcome, demonstrating that degraded PAR observations remain a valuable resource when properly upgraded.

b. Deployment and recovery

In situ comparisons should be performed at time of deployment and recovery with an accurate spectrophotometer containing a calibration traceable to the NIST or equivalent. The instrument should be left untouched during the comparison. The comparison might involve, for example, placing the traveling instrument in a bracket close to the weather station containing the Licor sensor.

c. Positioning the sensor

Guidelines are available to ensure that the instrument is positioned with a good sky view that is free of localized obstruction (WMO 2008). It is also recommended that the instruments be placed in simple gimbal platforms with a bubble level to ensure that sensing surfaces are kept as horizontal as possible and free from any movement in the supporting tower or pole.

d. Monitoring during deployment

Real-time monitoring of the data is available through the AIMS website (<https://weather.aims.gov.au>). Correction factors may be applied on a daily basis and the extent of signal deterioration may be followed throughout the season.

Significant events involving storms or other processes may be followed remotely. Correction ratios may indicate if there has been a catastrophic change in the signal or if the system is responding to solar forcing.

e. Shipboard observations

Practical considerations involving ship time may limit the number of visits for instrument replacement at each station site. A good alternative may involve concurrent shipboard measurements for a limited time at a location in close proximity. The results may be useful for comparison purposes, but it will depend on the weather and cloud characteristics for that particular day.

Acknowledgments. One of the authors (M. Nunez) received support from an AIMS Capability Development Fund research fellowship for this work. We gratefully acknowledge the help received from In-situ Marine Laboratories for providing spectral transmission and cosine responses of four Licor 192 quantum sensors. Data were sourced from the AIMS weather stations, Bureau of Meteorology, and Australia's Integrated Marine Observing System (IMOS) Lucinda Jetty Coastal Observatory. IMOS is enabled by the National Collaborative Research Infrastructure Strategy (NCRIS).

Data availability statement. All PAR data from weather stations and Satlantic Hypercor spectral radiometer used during this study are openly available at the Australian Institute of Marine Science data website: <https://www.aims.gov.au/docs/data/data.html>. Pyranometer data from Townsville Airport are available on request to the Australian Bureau of Meteorology: <http://www.bom.gov.au/climate/data-services/solar-information.shtml>.

APPENDIX

Quantum Irradiance to $W\ m^{-2}$

This appendix derives a correction factor C relating irradiance as measured in energy units ($W\ m^{-2}$) to quantum irradiance as measured in $\mu\text{mol}\ m^{-2}\ s^{-1}$. The energy of one photon (Ep) can be calculated as

$$\begin{aligned} E_p &= h\nu = h \frac{C}{\lambda} \\ &= \frac{6.62618 \times 10^{-34} \times 2.9979 \times 10^8\ \text{J s m s}^{-1}\text{m}^{-1} \times 10^9}{\lambda} (\lambda \text{ is in nm}) \\ &= \frac{19.86462}{\lambda} \times 10^{-17}\ \text{J}, \end{aligned}$$

where h = Planck constant = $6.62618 \times 10^{-34}\ \text{J s}$, ν = frequency (s^{-1}), and C = speed of light = $2.9979 \times 10^8\ \text{m s}^{-1}$.

For a given measure of energy, E_λ joules, the number of photons N is given by E_λ/E_p . Use 1 “mole” of light as a unit of measure, 1 mol = 6.02×10^{23} photons. Therefore, the number of photons equals $N/(6.02 \times 10^{23})$ moles, or $N/(6.02 \times 10^{17})$ micromoles.

So, for E joules, the number of micromoles is given by

$$\begin{aligned} \frac{\text{Number of photons}}{(\text{Avogadro's number} \times 10^{-6})} &= \frac{(E_\lambda/E_p)}{(6.02 \times 10^{23} \times 10^{-6})} \\ &= \frac{E_\lambda \lambda}{19.86462 \times 10^{-17} \times 6.02 \times 10^{23} \times 10^{-6}} = \frac{E_\lambda \lambda}{119.3850} \end{aligned}$$

For a specific wavelength range at steps of 1 nm with varying irradiance, we would have that PAR is given as

$$X\ \mu\text{mol}\ m^{-2}\ s = \int_{\lambda_1}^{\lambda_2} \frac{E(\lambda)\lambda}{119.58504} d\lambda \approx \sum_{i=1}^N \frac{E_i \lambda_i}{119.58504} \Delta\lambda,$$

where E_i is spectral irradiance ($W\ m^{-2}\ nm^{-1}$), $\lambda_1 = 400\ \text{nm}$, $\lambda_2 = 700\ \text{nm}$, and $\Delta\lambda$ is a wavelength interval of 1 nm.

A calibration factor is derived by comparing irradiance and quantum irradiance in the PAR using Libradtran 1.7 with cloudless conditions described in section 2b:

$$\underbrace{\int_{400}^{700} \left[\frac{E(\lambda, z)\lambda}{119.58504} \right] d\lambda}_{\text{Quantum irradiance } (\mu\text{mol}\ m^{-2}\ s^{-1})} = C \times \underbrace{\int_{400}^{700} E(\lambda, z) d\lambda}_{\text{Irradiance } (W\ m^{-2})},$$

where $E(\lambda, z)$ is spectral solar irradiance from Libradtran 2.0.4 for a particular wavelength and zenith angle combination and C is the desired calibration factor in $\mu\text{mol}\ m^{-2}\ s^{-1}\ (W\ m^{-2})^{-1}$.

The sensitivity of C to solar zenith angles changes is small, indicating a relatively small variation in the spectral distribution of solar radiation in the PAR wavelengths. A value of $4.57\ \mu\text{mol}\ m^{-2}\ s^{-1}\ (W\ m^{-2})^{-1}$ has been chosen with errors less than 0.20% for all solar zenith angles.

REFERENCES

- Arfken, G. B., H. J. Weber, and F. E. Harris, 2005: *Mathematical Methods for Physicists*. 6th ed. Academic Press, 1182 pp.
- Bainbridge, S. J., 2017: Temperature and light patterns at four reefs along the Great Barrier Reef during the 2015–2016 austral summer: Understanding patterns of observed coral bleaching. *J. Oper. Oceanogr.*, **10**, 16–29, <https://doi.org/10.1080/1755876X.2017.1290863>.
- Bergin, M. H., C. Ghoroy, D. Dixit, J. J. Schauer, and D. T. Shindell, 2017: Large reductions in solar energy production due to dust and particulate air pollution. *Environ. Sci. Technol. Lett.*, **4**, 339–344, <https://doi.org/10.1021/acs.estlett.7b00197>.
- Bird, R. E., 1984: A simple, solar spectral model for direct-normal and diffuse horizontal irradiance. *Sol. Energy*, **32**, 461–471, [https://doi.org/10.1016/0038-092X\(84\)90260-3](https://doi.org/10.1016/0038-092X(84)90260-3).
- Brando, V. E., J. L. Lovell, E. A. King, D. Boodle, R. Scott, and T. Schroeder, 2016: The potential of autonomous ship-borne hyperspectral radiometers for the validation of ocean color radiometry data. *Remote Sens.*, **8**, 150, <https://doi.org/10.3390/rs8020150>.
- Clack, C. T. M., 2017: Modeling solar irradiance and solar PV power output to create a resource assessment using linear multiple multivariate regression. *J. Appl. Meteor. Climatol.*, **56**, 109–125, <https://doi.org/10.1175/JAMC-D-16-0175.1>.
- De Soto, W., S. A. Klein, and W. A. Beckman, 2006: Improvement and validation of a model for photovoltaic array performance. *Sol. Energy*, **80**, 78–88, <https://doi.org/10.1016/j.solener.2005.06.010>.
- Dutton, E. G., J. J. Michalsky, T. Stoffel, B. W. Forgan, J. Hickey, D. W. Nelson, T. L. Alberta, and I. Reda, 2001: Measurements of broadband diffuse solar irradiance using current commercial instrumentation with a correction for thermal offset errors. *J. Atmos. Oceanic Technol.*, **18**, 297–314, [https://doi.org/10.1175/1520-0426\(2001\)018<0297:MOBDSI>2.0.CO;2](https://doi.org/10.1175/1520-0426(2001)018<0297:MOBDSI>2.0.CO;2).
- Feuermann, D., and A. Zemel, 1993: Dust-induced degradation of pyranometer sensitivity. *Sol. Energy*, **50**, 483–486, [https://doi.org/10.1016/0038-092X\(93\)90109-2](https://doi.org/10.1016/0038-092X(93)90109-2).
- Forgan, B. W., 1996: A new method for calibrating reference and field pyranometers. *J. Atmos. Oceanic Technol.*, **13**, 638–645, [https://doi.org/10.1175/1520-0426\(1996\)013<0638:ANMFCR>2.0.CO;2](https://doi.org/10.1175/1520-0426(1996)013<0638:ANMFCR>2.0.CO;2).
- Frouin, R., and R. T. Pinker, 1995: Estimating photosynthetically active radiation (PAR) at the Earth's surface from satellite observations. *Remote Sens. Environ.*, **51**, 98–107, [https://doi.org/10.1016/0034-4257\(94\)00068-X](https://doi.org/10.1016/0034-4257(94)00068-X).
- , and H. Murakami, 2007: Estimating photosynthetically available radiation at the ocean surface from ADEOS-II global imager data. *J. Oceanogr.*, **63**, 493–503, <https://doi.org/10.1007/s10872-007-0044-3>.
- , and Coauthors, 2018: Satellite radiation products for ocean biology and biogeochemistry: Needs, state-of-the-art, gaps, development priorities, and opportunities. *Front. Mar. Sci.*, **5**, 3, <https://doi.org/10.3389/fmars.2018.00003>.
- Gueymard, C. A., 1995: SMARTS2: A simple model of the atmospheric radiative transfer of sunshine: Algorithms and performance assessment. Florida Solar Energy Center Rep. FSEC-PF-270-95, 26 pp.
- , 2008: REST2: High-performance solar radiation model for cloudless-sky irradiance, illuminance, and photosynthetically active radiation—Validation with a benchmark dataset. *Sol. Energy*, **82**, 272–285, <https://doi.org/10.1016/j.solener.2007.04.008>.

- , J. M. Bright, D. Lingfors, A. Habte, and M. Sengupta, 2019: A posteriori clear-sky identification methods in solar irradiance time series: Review and preliminary validation using sky imagers. *Renewable Sustainable Energy Rev.*, **109**, 412–427, <https://doi.org/10.1016/j.rser.2019.04.027>.
- Habte, A., and M. Sengupta, 2016: Exploring sources of uncertainties in solar resource measurements. *Sixth PV Performance and Monitoring Workshop*, Freiburg, Germany, Fraunhofer ISE–Sandia National Laboratories, NREL/PR-5D00-67320, <https://www.nrel.gov/docs/fy17osti/67320.pdf>.
- Hill, K., T. Moltmann, R. Proctor, and S. Allen, 2010: The Australian Integrated Marine Observing System: Delivering data streams to address national and international research priorities. *Mar. Technol. Soc. J.*, **44**, 65–72, <https://doi.org/10.4031/MTSJ.44.6.13>.
- Iqbal, M., 1983: *An Introduction to Solar Radiation*. Academic Press, 390 pp.
- ISO, 1993: Solar energy-calibration of a pyranometer using a pyrheliometer. International Organization for Standardization Doc., 20 pp.
- , 2018: Solar energy-specification and classification of instruments for measuring hemispherical solar and direct solar radiation. International Organization for Standardization Doc., 18 pp.
- Janjai, S., S. Santaropas, and M. Nunez, 2009: Investigation of aerosol optical properties in Bangkok and suburbs. *Theor. Appl. Climatol.*, **96**, 221–233, <https://doi.org/10.1007/s00704-008-0026-4>.
- Jáuregui, E., and E. Luyando, 1999: Global radiation attenuation by air pollution and its effect on the thermal climate of Mexico City. *Int. J. Climatol.*, **19**, 683–694, [https://doi.org/10.1002/\(SICI\)1097-0088\(199905\)19:6<683::AID-JOC389>3.0.CO;2-8](https://doi.org/10.1002/(SICI)1097-0088(199905)19:6<683::AID-JOC389>3.0.CO;2-8).
- Ji, Q., 2007: A method to correct the thermal dome effect of pyranometers in selected historical irradiance measurements. *J. Atmos. Oceanic Technol.*, **24**, 529–536, <https://doi.org/10.1175/JTECH1977.1>.
- Jin, Z., T. P. Charlock, W. L. Smith Jr., and K. Rutledge, 2004: A parameterization of ocean surface albedo. *Geophys. Res. Lett.*, **31**, L22301, <https://doi.org/10.1029/2004GL021180>.
- Johnson, B. C., H. Yoon, J. P. Rice, and A. C. Parr, 2014: Principles of optical radiometry and measurement of uncertainty. *Optical Radiometry for Ocean Climate Measurement*, G. Zibordi, C. J. Donlon, and A. C. Parr, Eds., Experimental Methods in the Physical Sciences, Vol. 47, Elsevier, 13–67, <https://doi.org/10.1016/B978-0-12-417011-7.00003-9>.
- Jones, R., and Coauthors, 2020: Risk assessing dredging activities in shallow-water mesophotic reefs. Australian Institute of Marine Science Rep., 78 pp., <https://nesptropical.edu.au/wp-content/uploads/2020/03/NESP-TWQ-Project-2.1.9-Final-Report.pdf>.
- Kerr, J. P., G. W. Thurtell, and C. B. Tanner, 1967: An integrating pyranometer for climatological observer stations and meso-scale networks. *J. Appl. Meteor. Climatol.*, **6**, 688–694, [https://doi.org/10.1175/1520-0450\(1967\)006<0688:AIPFCO>2.0.CO;2](https://doi.org/10.1175/1520-0450(1967)006<0688:AIPFCO>2.0.CO;2).
- King, D. L., and D. R. Myers, 1997: Silicon-photodiode pyranometers: Operational characteristics, historical experiences, and new calibration procedures. *26th IEEE Photovoltaic Specialists Conf.*, Anaheim, CA, IEEE, <https://doi.org/10.1109/PVSC.1997.654323>.
- , W. E. Boyson, B. R. Hansen, and W. I. Bower, 1998: Improved accuracy for low cost solar irradiance sensors. *Second World Conf. and Exhibition on Photovoltaic Solar Energy Convention*, Vienna, Austria, EC Joint Research Centre.
- Kylling, A., A. Albold, and G. Seckmeyer, 1997: Transmittance of a cloud is wavelength-dependent in the UV-range: Physical interpretation. *Geophys. Res. Lett.*, **24**, 397–400, <https://doi.org/10.1029/97GL00111>.
- Licor, 1992: Instruction manual. LI-COR Doc., 28 pp.
- Long, C. N., and T. P. Ackerman, 2000: Identification of clear skies from broadband pyranometer measurements and calculation of downwelling shortwave cloud effects. *J. Geophys. Res.*, **105**, 15 609–15 626, <https://doi.org/10.1029/2000JD900077>.
- MacWhorter, M. A., and R. A. Weller, 1991: Error in measurements of incoming shortwave radiation made from ships and buoys. *J. Atmos. Oceanic Technol.*, **8**, 108–117, [https://doi.org/10.1175/1520-0426\(1991\)008<0108:EIMOIS>2.0.CO;2](https://doi.org/10.1175/1520-0426(1991)008<0108:EIMOIS>2.0.CO;2).
- Madhavan, B. L., H. Deneke, J. Witthuhn, and A. Macke, 2017: Multiresolution analysis of the spatiotemporal variability in global radiation observed by a dense network of 99 pyranometers. *Atmos. Chem. Phys.*, **17**, 3317–3338, <https://doi.org/10.5194/acp-17-3317-2017>.
- Mant, M., and R. Pillai, 2010: Impact of dust on solar photovoltaic (PV) performance: Research status, challenges and recommendations. *Renewable Sustainable Energy Rev.*, **14**, 3124–3131, <https://doi.org/10.1016/j.rser.2010.07.065>.
- Masiri, M., M. Nunez, and E. Weller, 2007: A ten-year solar radiation climatology of the Great Barrier Reef: Implications for recent mass coral bleaching events. *Int. J. Remote Sens.*, **15**, 4443–4462, <https://doi.org/10.1080/01431160801930255>.
- Mayer, B., and A. Kylling, 2005: The libRadtran software package for radiative transfer calculations—Description and examples of use. *Atmos. Chem. Phys.*, **5**, 1855–1877, <https://doi.org/10.5194/acp-5-1855-2005>.
- , —, C. Emde, R. Buras, U. Hamann, J. Gasteiger, and B. Richter, 2020: libRadtran user's guide: Version 2.0.4. libRadtran Doc., 138 pp.
- McPherson, H. G., 1969: Photocell-filter combinations for measuring photo-synthetically active radiation. *Agric. Meteor.*, **6**, 347–356, [https://doi.org/10.1016/0002-1571\(69\)90026-0](https://doi.org/10.1016/0002-1571(69)90026-0).
- Menyhart, L., A. Anda, and Z. Nagy, 2015: A new method for checking the levelling of pyranometers. *Sol. Energy*, **120**, 25–34, <https://doi.org/10.1016/j.solener.2015.06.033>.
- Michalsky, J. J., R. Perez, L. Harrison, and B. A. LeBaron, 1991: Spectral and temperature correction of silicon photovoltaic solar radiation collectors. *Sol. Energy*, **47**, 299–305, [https://doi.org/10.1016/0038-092X\(91\)90121-C](https://doi.org/10.1016/0038-092X(91)90121-C).
- , L. C. Harrison, and W. E. Berkheiser, 1995: Cosine response characteristics of some radiometric and photometric sensors. *Sol. Energy*, **54**, 397–402, [https://doi.org/10.1016/0038-092X\(95\)00017-L](https://doi.org/10.1016/0038-092X(95)00017-L).
- Mondol, J. D., Y. G. Yohanis, and B. Norton, 2008: Solar radiation modelling for the simulation of photovoltaic systems. *Renewable Energy*, **33**, 1109–1120, <https://doi.org/10.1016/j.renene.2007.06.005>.
- Myers, D. R., 2005: Solar radiation modeling and measurements for renewable energy applications: Data and model quality. *Energy*, **30**, 1517–1531, <https://doi.org/10.1016/j.energy.2004.04.034>.
- Nunez, M., 1993: The development of a satellite-based insolation model for the tropical western Pacific Ocean. *Int. J. Climatol.*, **13**, 607–627, <https://doi.org/10.1002/joc.3370130603>.
- , K. Fienberg, and C. Kuchinke, 2005: Temporal structure of the solar radiation field in cloudy conditions: Are retrievals

- of hourly averages from space possible? *J. Appl. Meteor.*, **44**, 167–185, <https://doi.org/10.1175/JAM-2196.1>.
- , M. J. Marin, D. Serrano, M. P. Utrillas, K. Fienberg, and J. A. Martinez-Lozano, 2016: Sensitivity of UVER enhancement to broken liquid water clouds: A Monte Carlo approach. *J. Geophys. Res. Atmos.*, **121**, 949–964, <https://doi.org/10.1002/2015JD024000>.
- Patil, A., K. Haria, and P. Pashte, 2013: Photodiode based pyranometer. *Int. J. Adv. Sci. Eng. Inf. Technol.*, **1**, 29–33.
- Payne, R. E., 1972: Albedo of the sea surface. *J. Atmos. Sci.*, **29**, 959–970, [https://doi.org/10.1175/1520-0469\(1972\)029<0959:AOTSS>2.0.CO;2](https://doi.org/10.1175/1520-0469(1972)029<0959:AOTSS>2.0.CO;2).
- Perez, R., R. Seals, P. Ineichen, R. Stewart, and D. Menicucci, 1987: A new simplified version of the Perez diffuse irradiance model for tilted surfaces. *Sol. Energy*, **39**, 221–231, [https://doi.org/10.1016/S0038-092X\(87\)80031-2](https://doi.org/10.1016/S0038-092X(87)80031-2).
- Raich, A., J. A. Gonzalez, and J. Calbo, 2007: Effects of solar height, cloudiness and temperature on silicon pyranometer measurements. *Tethys*, **4**, 11–18, <https://doi.org/10.3369/tethys.2007.4.02>.
- Razagui, A., K. Abdeladim, A. H. Arab, and S. Boulachiche, 2020: Modeling the forecasted power of a photovoltaic generator using numerical weather prediction and radiative transfer models coupled with a behavioral electrical model. *Energy Rep.*, **6**, 57–62, <https://doi.org/10.1016/j.egy.2019.08.018>.
- Reno, M. J., and C. W. Hansen, 2016: Identification of periods of clear sky irradiance in time series of GHI measurements. *Renewable Energy*, **90**, 520–531, <https://doi.org/10.1016/j.renene.2015.12.031>.
- Robson, B., and Coauthors, 2020: Benthic light as an ecologically-validated GBR-wide indicator for water quality. Australian Institute of Marine Science Rep., 40 pp., <https://nesptropical.edu.au/wp-content/uploads/2019/07/NESP-TWQ-Project-2.3.1-Final-Technical-Report.pdf>.
- Ross, J., and M. Sulev, 2000: Sources of error in measurements of PAR. *Agric. For. Meteorol.*, **100**, 103–125, [https://doi.org/10.1016/S0168-1923\(99\)00144-6](https://doi.org/10.1016/S0168-1923(99)00144-6).
- Schenk, H., T. Hirsch, M. Wittmann, S. Wilbert, L. Keller, and C. Prah, 2015: Design of an irradiance measurement network. *Energy Procedia*, **69**, 2019–2030, <https://doi.org/10.1016/j.egypro.2015.03.212>.
- Serrano, D., M. J. Marin, M. Nunez, M. P. Utrillas, S. Gandia, and J. A. Martinez-Lozano, 2015: Wavelength dependence of the effective cloud optical depth. *J. Atmos. Sol.-Terr. Phys.*, **130–131**, 14–22, <https://doi.org/10.1016/j.jastp.2015.05.001>.
- Shettle, E., 1989: Models of aerosols, clouds and precipitation for atmospheric propagation studies. *Proc. AGARD Conf. on Atmospheric Propagation in the UV, Visible, IR and MM-Region and Related System Aspects*, Copenhagen, Denmark, Advisory Group for Aerospace Research and Development, 1–13.
- Stephens, G., 1994: *Remote Sensing of the Lower Atmosphere: An Introduction*. Oxford University Press, 523 pp.
- Utrillas, M. P., J. V. Boscá, J. A. Martínez-Lozano, J. Cañada, F. Tena, and J. M. Pinazo, 1998: A comparative study of SPECTRAL2 and SMARTS2 parameterized models based on spectral irradiance measurements at Valencia, Spain. *Sol. Energy*, **63**, 161–171, [https://doi.org/10.1016/S0038-092X\(98\)00058-9](https://doi.org/10.1016/S0038-092X(98)00058-9).
- Van Laake, P. E., and G. A. Sanchez-Azofeifa, 2005: Mapping PAR using MODIS atmosphere products. *Remote Sens. Environ.*, **94**, 554–563, <https://doi.org/10.1016/j.rse.2004.11.011>.
- WMO, 2008: Guide to meteorological instruments and methods of observation. 7th ed. WMO Doc., 681 pp.
- Young, H. D., 1962: *Statistical Treatment of Experimental Data*. McGraw-Hill, 172 pp.